JGR Atmospheres

Key Points:

- There is evidence for the simultaneous and collocated presence of mountain waves and non-orographic gravity waves during a SOUTHTRAC flight
- MW dominated above sharp topography in Southern Patagonia and southeastwards. NOGW predominated above the oceans
- WRF simulations up to the mesosphere against onboard-based observations show good GW representation in temperature perturbations and fair in vertical velocity

The Coexistence of Gravity Waves From Diverse Sources During a SOUTHTRAC Flight

P. Alexander[1] [ID], A. de la Torre[2] [ID], P. Llamedo[2], R. Hierro[2], T. Marcos[2] [ID], B. Kaifler[3] [ID], N. Kaifler[3] [ID], M. Geldenhuys[4] [ID], P. Preusse[4], A. Giez[5], M. Rapp[3], and J. L. Hormaechea[6] [ID]

[1]Instituto de Física de Buenos Aires, CONICET, Ciudad Universitaria Pabellón 1, Buenos Aires, Argentina, [2]LIDTUA, Facultad de Ingeniería, Universidad Austral and CONICET, Pilar, Argentina, [3]Institute of Atmospheric Physics, German Aerospace Center, Oberpfaffenhofen, Germany, [4]Institute of Energy and Climate Research (IEK-7), Forschungszentrum Jülich, Jülich, Germany, [5]Einrichtung Flugexperimente, German Aerospace Center, Oberpfaffenhofen, Germany, [6]Estación Astronómica Río Grande, Facultad de Ciencias Astronómicas y Geofísicas, Universidad Nacional de La Plata and CONICET, Buenos Aires, Argentina

Abstract We use observations from one of the SOUTHTRAC (Southern Hemisphere Transport, Dynamics, and Chemistry) Campaign flights in Patagonia and the Antarctic Peninsula during September 2019 to analyze possible sources of gravity waves (GW) in this hotspot during austral late winter and early spring. Data from two of the instruments onboard the German High Altitude and Long Range Research Aircraft (HALO) are employed: the Airborne Lidar for Middle Atmosphere research (ALIMA) and the Basic HALO Measurement and Sensor System (BAHAMAS). The former provides vertical temperature profiles along the trajectory, while the latter gives the three components of velocity, pressure, and temperature at the flight position. GW-induced perturbations are obtained from these observations. We include numerical simulations from the Weather Research and Forecast (WRF) model to place a four-dimensional context for the GW observed during the flight and to present possible interpretations of the measurements, for example, the orientation or eventual propagation sense of the waves may not be inferred using only data obtained onboard. We first evaluate agreements and discrepancies between the model outcomes and the observations. This allowed us an assessment of the WRF performance in the generation, propagation, and eventual dissipation of diverse types of GW through the troposphere, stratosphere, and lower mesosphere. We then analyze the coexistence and interplay of mountain waves (MW) and non-orographic (NO) GW. The MW dominate above topographic areas and in the direction of the so-called GW belt, whereas the latter waves are mainly relevant above oceanic zones. WRF simulates NOGW as mainly upward propagating entities above the lower stratosphere. Model runs show that deep vertical propagation conditions are in general favorable during this flight but also that in the upper stratosphere and lower mesosphere and mainly above topography there is some potential for wave breaking. The numerical simulations evaluate the GW drag for the whole flight area and find that the strongest effect is located in the zonal component around the stratopause. The general behavior against height resembles that obtained with a local fixed lidar data. According to WRF results, up to 100 km horizontal wavelength MW account for about half of the force opposing the circulation of the atmosphere.

Plain Language Summary We use observations from one of the SOUTHTRAC (Southern Hemisphere Transport, Dynamics, and Chemistry) Campaign flights in Patagonia and the Antarctic Peninsula during September 2019 to analyze possible sources of atmospheric waves. Data from two of the cutting-edge instruments onboard the German High Altitude and Long Range Research Aircraft (HALO) are employed. They provide velocity, pressure, and temperature at the flight position and above. We include numerical simulations to place a four-dimensional context for the waves observed during the flight. Agreements and discrepancies between the model outcomes and the observations are evaluated. We then analyze the coexistence of waves generated by the mountains and other sources.

1. Introduction

Gravity waves (GWs) and the large-scale planetary waves and tides are the main drivers for the general circulation of the middle atmosphere. The primary sources of GW are topography, convection, fronts, instabilities, and spontaneous adjustment (e.g., Fritts & Alexander, 2003). GW constitute an important dynamical coupling mechanism between different regions and layers of the atmosphere by redistributing energy and momentum over

large horizontal and vertical distances. They may transport both quantities away from the source area and release them in another zone during their dissipation. The deposition of momentum generates the GW drag which may accelerate, decelerate or sometimes even reverse the mean flow. An adequate representation of this drag in global circulation models is a key feature for realistic descriptions of the dynamical and thermal structure of the atmosphere. However, a significant part of the drag is due to small-scale GW and is not resolved by numerical models, which implies that their effect has to be parameterized through theoretical or observational means. Moreover, it has been shown that analysis or reanalysis data-sets cannot in general resolve GW horizontal wavelengths smaller than about 200 km (Preusse et al., 2014).

General circulation models usually produce in the middle atmosphere around 60°S a too low GW drag (McLandress et al., 2012) during austral late winter and early spring. This leads in the stratosphere to stronger circumpolar winds and lower temperatures within the vortex than usually observed. Diverse causes have been suggested for the missing drag in the numerical models: large amplitude and short horizontal wavelength GW generated over the continental Andes and the Antarctic Peninsula and their downwind advection and meridional refraction into the polar night jet (e.g., Sato et al., 2012), mountain waves (MW) from small islands in the area which are not well-resolved by the numerical models (e.g., Hoffmann et al., 2016), secondary GW generated by the breaking of orographic waves (e.g., Satomura & Sato, 1999), GW related to winter storm tracks over the southern oceans (e.g., Hendricks et al., 2014; Plougonven et al., 2015) and spontaneous adjustment and instability around the polar night jet (e.g., Hindley et al., 2015; Geldenhuys et al., 2021).

The study by McLandress et al. (2012) showed that the models produced large zonal winds around 60°S mainly located between 3 and 1 hPa. They also made numerical experiments with drag artificially added around that latitude and obtained more realistic stratospheric winds and temperatures. Garcia et al. (2017) followed a similar procedure and also obtained improvements around the Antarctic polar vortex, and thereafter tested the effects of artificial non-orographic gravity waves (NOGW) which also led to better results. They therefore concluded that careful examination of observational evidence and model performance was required to establish which GW sources really produced the observed drag correction.

Most of the experiments and campaigns on GW in the lower and middle atmosphere usually focus on the Northern Hemisphere probably due to operational reasons. However, observations and model data indicate significant differences between both hemispheres. For example, a possible source of waves like the polar vortex is stronger and more persistent in the Southern Hemisphere (Schoeberl & Newman, 2015). Global observations of GW exhibit several regions of large GW momentum flux around the planet (e.g., Ern et al., 2017, 2018; Hoffmann et al., 2013, 2016). The region which seems to show the largest values encompasses the southern continental Andes and the Antarctic Peninsula (e.g., Ern et al., 2004, 2018). The geographical area possesses steep topography and strong horizontal winds, which are favorable conditions to excite intense GW. Therefore the region attracted for over one decade several satellite and ground-based instrumentation studies (e.g., Alexander et al., 2010; de la Torre et al., 2012; Kaifler & Kaifler, 2021; Llamedo et al., 2019; Reichert et al., 2021; Wright et al., 2016; Zhao et al., 2017). Another GW hotspot region may be found around New Zealand. The Deep Propagating Gravity Wave Experiment (DEEPWAVE) during the austral winter of 2014 was the first extensive observational campaign in the Southern Hemisphere devoted to the study of the generation, propagation, and dissipation of GW (e.g., Fritts et al., 2016). All these facts have been highlighting the research potential of a multi-platform study around the tip of South America.

The SOUTHTRAC (Southern Hemisphere Transport, Dynamics, and Chemistry) campaign took place in the hotspot around the Southern Andes and the Antarctic Peninsula during the late austral winter and early spring in 2019 (Rapp et al., 2021). The lidar system ALIMA (Airborne Lidar for Studying the Middle Atmosphere) flew for the first time on HALO (High Altitude and Long Range Research Aircraft). This is an upward-looking instrument that provides temperatures from approximately flight level (usually about 12 km) up to 80 km altitude (e.g., Kaifler et al., 2017). The Basis HALO Measurement and Sensor System (BAHAMAS) recorded onboard high-frequency (100 Hz) in-situ measurements of position and the three components of atmospheric velocity, temperature, and pressure (Giez et al., 2017, 2021). The ST08 flight departed from Río Grande around 23 UTC on September 11, 2019, and landed in the same airport about 8 hr later. An initial analysis of the flight observations revealed a rich interplay of phenomena: the existence of large-amplitude GW, their deep upward propagation and breaking, the possible presence of secondary waves, refraction into the polar night jet and along the so-called GW belt, and the superposition of wave modes (Rapp et al., 2021). Around topography, a complex mixture of

GW at various scales may be seen. The onboard cutting-edge instruments may allow the unprecedented in-situ observation of details in a zone that hosts intense GW with a variety of possible origins not yet fully clarified.

Preliminary SOUTHTRAC results mentioned above show strong and complex GW activity hinting at the simultaneous presence of multiple sources. Below we try to locate and separate MW from NOGW and we intend to find some hints on the possible origin of the latter. We focus on some of the possible NOGW sources already mentioned for the missing drag. Uccellini and Koch (1987) found that one possible source for inertia GW is the geostrophic adjustment associated with jet streaks. Plougonven et al. (2003) and Plougonven and Zhang (2014) mentioned significant inertia GW close to the jet axis and mainly around the maximum or the regions of strong curvature and concluded that they were due to geostrophic adjustment or in other words spontaneous emission. Or even the jet itself (Becker et al., 2022) or its interaction with orography (Geldenhuys et al., 2021) or with MW (de la Torre et al., 2006) can lead to the excitation of GW. Therefore the polar night jet is a candidate for NOGW generation player, but not the only one. Cold fronts (Fritts & Alexander, 2003) and MW breaking due to convective or dynamic instability (Plougonven et al., 2008) are also possible mechanisms in this region.

This work should be considered complementary to de la Torre et al. (2023). For a scenario with complex mixtures of packets of GW, the spectral method that they applied may be used in order to identify dominant wave aspects. The study is rather qualitative than quantitative, as it obtains statistical information on prevailing up- or down-propagating wave energy flux based only on the dominant polarization degree of detected modes. That work uses analysis data coincident with flight ST08 with a rotary spectral technique and compares the results with observations, whereas the present study uses an approach with mesoscale simulations. They also used polarization results based on the analysis data corresponding to the time and area covered by the airplane to develop a classification of the present GW according to their orographic or non-orographic origin. Results indicate a possible mixed presence of types of GW in the studied region. Linearly polarized (possible MW) are detected close to mountains and also in some limited oceanic areas. In the troposphere and lower stratosphere above some zones, a predominance of downwards wave energy flux was observed. As MW produce upward wave energy propagation, this indicates the possible relevance of NOGW in the studied region. The calculated upward wave energy flux rises as expected close to mountains and also in some limited oceanic areas. Above the lower stratosphere, the wave energy flux is much larger than below, providing evidence in that layer for the presence of NOGW sources. Throughout the whole altitude interval there are upward and downward wave energy fluxes from possible MW and NOGW, with some departures from linear polarization and very complex patterns and interplay between both types of waves. In the present work, we confirm some of these statements from the perspective of a mesoscale model and also find some discrepancies. We should recall that we refer here specifically to the wave energy flux and not to the total perturbation energy flux (Hines & Reddy, 1967; Lindzen, 1973), which includes a coupling term between the mean flow and a wave. For conservative MW that are stationary in a ground-based reference system, the wave energy flux is positive but the total component is null (Becker & Vadas, 2018).

The simultaneous use of measurements and the Weather Research and Forecasting (WRF) numerical model may provide a fruitful combination of tools in order to unmask the complex combination of phenomena that may be present during the GW hotspot high-season. In particular, the numerical simulations may help to provide in the present work a spatial and temporal context of GW and their background around flight ST08 and may offer possible clues on the sources and evolution of the waves observed by onboard instruments. For example, information on the relative orientation between GW fronts and aircraft trajectory or real (not apparent as seen from HALO) horizontal wavelengths may be obtained from the model. Comparisons between onboard-based measurements and WRF may also allow a validation of the model and its settings over complex orography and up to the mesosphere.

In Section 2, we provide details about the data from the campaign instruments and from the numerical simulations performed for the flight and the tools for their processing. In Section 3, we review the atmospheric conditions before and during the flight. In Section 4, the mesoscale model becomes validated against the data from onboard instruments. Section 5 shows the results and their interpretation. Diagnostics based on linear and non-linear theory (polarization relations, links between wave energy and momentum fluxes, Richardson number, etc.) will be obtained with WRF data and will be used for a quantitative and qualitative analysis and interpretation of the scenario around the flight. It is our aim to disentangle the different contributions to GW activity observed during a flight with outstanding excitation and propagation conditions to possibly connect signatures and sources. Numerical simulations will also be used to assess the relative relevances of MW and NOGW in the drag along the

flight path and over the whole area. The relative contributions to the drag of GW with short and long horizontal wavelength are also evaluated. In Section 6, we discuss some results and draw our conclusions.

2. Observations, Simulations, and Data Processing

2.1. Onboard Instruments

ALIMA is an upward-pointing Rayleigh lidar system for airborne measurements using a pulsed neodymium-doped yttrium aluminum garnet laser transmitting 12.5 W at 532 nm with a 48-cm diameter receiving telescope, and using three height-cascaded elastic detector channels (e.g., Kaifler et al., 2017). Optical filters inserted in the optical path in front of the photon detectors suppress the broadband solar background and thus allow for observations in full daylight. An active beam stabilization system analyzes and corrects the alignment of the laser beams after each laser pulse, maintaining a precise lock of the beams to the field of view of the telescope even during aircraft maneuvers and the occurrence of turbulence. Density is first obtained and then transformed into temperature using hydrostatic downward integration in the 20–90 km height interval. To isolate GW temperature oscillations, a 30-min running mean (at typical flight speed it corresponds to about 420 km) is used as a representation of the background. The temporal resolution of 2 min (a rough aircraft displacement of 30 km) allows the detection of short horizontal wavelength GW, which supposedly make a significant contribution to the GW momentum flux. Profiles with 1 min resolution may be also available with somewhat larger uncertainties.

The BAHAMAS measurement system consists of a nose tip probe setup on HALO with a 5-hole wind sensor and provides in situ measurements of both horizontal and vertical wind components as well as temperature and pressure and other physical quantities at flight altitude at a temporal resolution of 100 Hz (e.g., Giez et al., 2017). Most SOUTHTRAC segments have been processed at 10 Hz as the corresponding horizontal scale is adequate for GW studies. The highest resolution data is usually used for turbulence analysis (e.g., Dörnbrack et al., 2022).

2.2. Numerical Model Settings

Numerical high-resolution simulations were performed with the 4.2 version of the WRF model (Skamarock & Klemp, 2008) forced with initial and boundary conditions from the National Centers for Environmental Prediction/Global Data Assimilation System (NCEP/GDAS) 0.25° × 0.25° global final analyses, which are provided every 6 hr. The data are available at 34 levels from 1,000 to 1 hPa (roughly 42 km height). This solution was not used for any calculations or figures below unless otherwise stated. It just remained as a control simulation for tests in the coincident height interval against a run reaching the lower mesosphere as described in the next paragraph. There were just minor discrepancies between both results. The application of WRF to a region with very sharp topography and to the simulation of the generation, propagation, and dissipation of the corresponding GW is a significant challenge. An adequate choice of numerical time step, horizontal and vertical resolution, physical parameterizations, domain locations, and the tuning of diverse model coefficients becomes mandatory for a successful run. Three nested domains (d01, d02, and d03) were used in the flight area at 9, 3, and 1 km horizontal resolutions, respectively (see Figure 1). The three grid sizes are respectively (W-E × S-N) 364 × 382, 697 × 574, and 805 × 643 points. Figure 1 also shows the aircraft trajectory during flight ST08. The two largest computational domains fully contain the flight, whereas the smallest one is focused on a region with large amplitude MW. A Rayleigh damping layer was placed in the upper 10 km to attenuate GW reflection effects at the model lid (so simulations are affected by artificial diffusion from 32 to 42 km height). A time step of 36 s was chosen for the largest domain and scaled appropriately for the inner nests. The simulation started on September 11 at 00 UTC and ended 36 hr later. To allow for model spin-up, the simulations were used only 23 hr after the initial conditions. The physical parameterizations that were used are: microphysics (WSM 3-class simple ice scheme), shortwave and longwave radiation scheme (RRTMG), surface and boundary layer (Quasi-Normal Scale Elimination), land surface model (Unified Noah), and no cumulus scheme (it is assumed that the model is capable of producing it at the used resolutions). Model terrain height within domains was derived from the 30 s digital elevation model distributed with WRF. This was bilinearly interpolated onto the model grid. WRF outputs were provided every 6 min to adequately reproduce non-steady features and for comparison with high-resolution onboard measurements. This reference simulation has 90 vertical levels, whereby the coarsest resolution is around 600 m close to the model top at 1 hPa.

The inclusion of the stratosphere and mesosphere poses additional complications for the numerical model. We developed WRF simulations up to a model top of 0.01 hPa (roughly 75 km height) with ERA5 (fifth generation
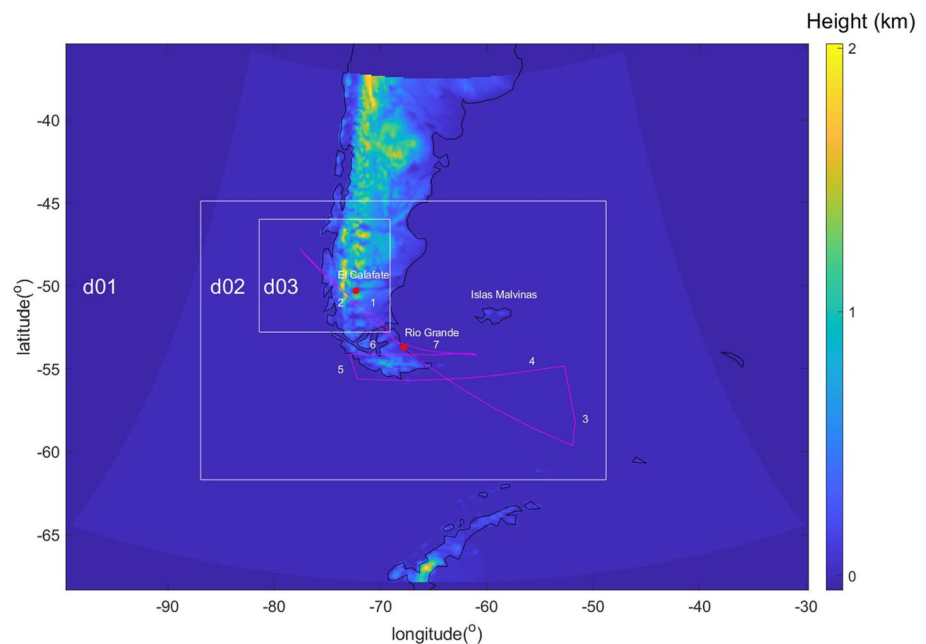
Figure 1. The ST08 flight trajectory in magenta color lines and the increasing numbers associated with each leg according to the airplane sequence are shown. So leg 1 corresponds to the segment after departure from Río Grande and leg 7 represents the last flight path before landing in the same city. The three nested domains d01, d02, and d03 used with the WRF numerical model are included. For clarity, the Lambert projection used in the simulations is only drawn for the largest zone. Its general shape is the same in the other two domains.

European Centre for Medium-Range Weather Forecasts atmospheric reanalysis) forcing data with 137 levels every hour and $0.30° \times 0.30°$ horizontal resolution. We now repeated the previous setups for horizontal grid sizes and resolutions and physical parameterizations for domains d01 and d02. Simulation start and spin-up interval are also copied, whereby the run ended on September 12 at 07 UTC. A time step of 15 s was chosen for the largest domain and the damping sponge was placed in the upper 15 km. This means that solutions were usable up to 60 km altitude. A shorter time step had to be now used to avoid numerical instabilities in the domain borders at high altitudes. The simulation possesses 150 vertical levels, whereby the coarsest resolution is 800 m close to the top. WRF outputs were provided every 15 min. Comparisons of the first and second runs in the 0–32 km height range lead to minor differences (not shown) providing a fair validation for an adequate functioning of deep WRF, at least in the lower half of the full altitude interval. The d02 files for the three components of velocity, temperature, and pressure just for 8 hr of the flight with 120 levels up to 60 km height (the usable altitude range of solutions) occupy a space on disk of 150 GB.

The numerical simulations will be compared below against observations collected on board the HALO aircraft to validate WRF results. Model quantities from domains d02 and d03 were linearly interpolated in space and time to every HALO measurement. In Figure 1, we see the definition of the flight leg numbers. Each segment is essentially straight and stays at constant pressure with height changes within 500 m along several 100 km and no steep ascents, descents, or turns. In this study, we concentrated on legs 1, 2, 4, and 6. The first two segments are essentially diagonal flights in opposite direction over Southern Patagonia including the Andes, and the remaining two are nearly constant latitude trajectories with inverted sense above the Tierra del Fuego island area. These characteristics make these pairs of legs potentially comparable and in addition they cover a large fraction of the flight. In the figure, we also show the location of Río Grande city, whose airport was used for departure and landing in all flights and El Calafate, whose surroundings are considered to be an intense MW hotspot (e.g., de la Torre et al., 2012; Kaifler et al., 2020; Wright et al., 2016).

2.3. GW Interpretation Tools

Oscillations of a GW happen in all three wind components as well as in density and pressure (and thus temperature) at the same frequency and three cartesian wavenumbers. There are magnitude and phase shifts between

those quantities provided by the so-called polarization relations (e.g., Gill, 1982; Fritts & Alexander, 2003; Vadas, 2013) within linear theory. For the complex amplitudes $\tilde{u}$, $\tilde{v}$ of the zonal and meridional perturbation velocity components du and dv

$$\tilde{u} = \left(\frac{i\hat{\omega}k - fl}{i\hat{\omega}l + fk} \right) \tilde{v} \tag{1}$$

where $\hat{\omega}, f$ refer to the wave intrinsic and inertial frequencies and k, l correspond to the zonal and meridional wave number components. From Equation 1, in the general case, an ellipse links both horizontal velocity amplitudes, whereby the eccentricity indicates the ratio of inertial to GW intrinsic frequency. In addition, the orientation of the major axis shows the direction of horizontal phase propagation within a 180° ambiguity. At Andes, the typical wind speeds that traverse the topography width define an intrinsic frequency range well above the inertial value and thereby lead to a simplified polarization relation (Vadas et al., 2018)

$$\tilde{u} = \frac{k}{l} \tilde{v} \tag{2}$$

so there is a nearly linear relation between both components and MW phase differences between u and v stay around 0° or 180°. For example, Plougonven et al. (2008) used this polarization relation to study an MW over the Antarctic Peninsula. However, it should be recalled that certain orography can even generate inertia-GW (e.g., Dörnbrack et al., 2002; Queney, 1948).

For a GW with a vertical wavelength much smaller than 4π times the density scale height, there is also a simple polarization relation between the complex amplitudes of the perturbations in temperature $\tilde{T}$ and vertical velocity $\tilde{w}$ as shown by Vadas (2013).

$$\tilde{T} = \frac{iN^2}{g\hat{\omega}} \tilde{w}. \tag{3}$$

Here N and g are, respectively, the Brunt-Väisälä frequency and gravity and it is clear that both components stay in quadrature. These polarization relations will be used below to test the existence of GW in WRF domain d02 simulations or observational data and if they are present, then the expressions will be applied to scrutinize if they are MW or NOGW.

According to Equation 2, high intrinsic frequency MW should exhibit a nearly linear relationship between the two horizontal velocity perturbation components. We set a range of 0° or 180° ± 180°/10 phase difference range for them, whereby outside of this interval waves are considered to be elliptically polarized. In addition to this distinction, MW are required to exhibit vertical wavelengths between 5 and 20 km and NOGW between 2.5 and 5 km. This separation is justified by results shown below and by Ehard et al. (2015) and Reichert et al. (2021). However, we are aware that this is a simplified picture as MW can have lower vertical wavelengths and NOGW like secondary waves can have larger values (e.g., Becker & Vadas, 2018; Vadas & Becker, 2018, 2019). In addition, we require that MW signatures are present for a minimum of one vertical wavelength and NOGW for four vertical wavelengths (at least four complete elliptical turns of the horizontal velocity perturbation should appear in a hodograph). The last condition could be to severe and may lead to miss some waves but it ensures that we will capture clear cases. We will use wavelet coherence along vertical columns above each grid point from the ground to 60 km height of u and v data to find the regions where both perturbation components very likely exhibit an associated behavior (magnitude-squared coherence larger than a given cutoff) at given times. A strict coherence cutoff is needed to have a clear identification of characteristic areas. Above every point of the grid, the vertical wavelengths are determined from the wavelet scales and the height ranges for the existence of GW fingerprints are identified by the coherence staying above a given cutoff. Phase differences between both signals are found from the wavelet cross-spectrum. If, at any geographical point, there are two different GW types (MW and NOGW) at two different height intervals, then only the one with the strongest coherence is kept.

The phase difference between any two related signals is analyzed by wavelet coherence and cross-spectrum (e.g., Grinsted et al., 2004; Torrence & Compo, 1998). The magnitude-squared wavelet coherence is a measure of localized correlation between two data series in the time-frequency or distance-wavenumber domains. This tool is useful for analyzing non-stationary or non-uniform signals and constraining the location of certain phenomena in time and frequency or distance and wavenumber planes. The coherence is computed here using the Morlet

wavelet. The magnitude-squared wavelet coherence of two signals x_1 and x_2 with continuous wavelet transforms $W_1(a, b)$, and $W_2(a, b)$ at scale a and position b is given by

$$\frac{|S\left(W_1(a, b)^* W_2(a, b)\right)|^2}{S(|W_1(a, b)|^2) S(|W_2(a, b)|^2)}$$

whereby * is complex conjugate and S is a smoothing operator in time (or distance) and scale which should be determined according to the observed coherence noisiness. The phase obtained from the wavelet cross-spectrum, which is a measure of the distribution of the power in the two signals, is employed to infer the relative lag between common modes in both data series. The expression for the wavelet cross-spectrum at scale a and position b is

$$S\left(W_1(a, b)^* W_2(a, b)\right).$$

Notice that no filtering needs to be applied to the signals x_1 and x_2 as the wavelets are already doing the job of selecting the scales and comparing them.

3. Meteorological and Dynamic Conditions During Flight ST08

The synoptic conditions during the flight time and region have been discussed by de la Torre et al. (2023) and are briefly recalled here. Dörnbrack et al. (2020) also outline some meteorological aspects around El Calafate to the lee of Andes and within its area but a few hours before flight ST08. There was a low-pressure level system near surface located to the East of the Antarctic Peninsula on September 11, 18 UTC. It was associated with a cold front. The equivalent potential temperature gradient and the strong winds from SW at 850 hPA indicated the presence of incoming cold air above Southern Patagonia. A Pacific anticyclone around 55°S carried polar air over the Drake passage. As a result, there was a strong low-level wind blowing from SW over the Tierra del Fuego island, whereas a predominant westerly flow was present above Patagonia. After 12 hr, the Pacific anti-cyclone reached the continent while the low-level pressure system and the front moved to the East. This resulted in a weakening of the low-level wind over the land but kept similar intensity winds over the Drake passage. In Figure 2, we can see the mesoscale scenario for GW propagation obtained from NCEP/GDAS 1° × 1° global final analyses. According to panels (a–f), there is mainly an SW wind (angles between −180° and −90°) present at mountain altitudes in the region, with large values from the surface to the upper levels. This scenario provides optimal conditions for MW generation and deep propagation. Some irregular behavior in the angles at low heights at some latitudes is due to the close presence of topography to the East, which prevents them in some areas below 300 hPa from staying between −90° and 90°.

As a proxy for the jet as a possible source of NOGW, in panel (g) of Figure 2, we can see the horizontal wind magnitude and the location of the polar vortex edge. The equivalent latitude represents the latitude that an air mass would have if the polar vortex was centered at the South Pole. It allows a characterization of an air mass in terms of its location relative to the polar vortex rather than in relation to the geographical latitude. The equivalent latitude corresponding to the edge can be calculated from potential vorticity. The vortex edge was derived through the equivalent latitude of the largest potential vorticity gradient weighted by the horizontal wind speed (Nash et al., 1996) on September 11, 18 UTC and September 12, 00 and 06 UTC. ERA5 data have been used at 475K isentropic level (roughly 19 km height). HALO may have spent part of its journey inside or under the vortex. The Southern polar vortex was displaced toward the tip of South America and broke down early during the late austral winter of 2019 due to a sudden stratospheric warming (Dörnbrack et al., 2020). This restricted the propagation above 40 km height for MW in the hotspot area as of September 13th, while low-level conditions stayed optimal for their forcing. As a consequence, ST08 could have been the only flight of the campaign with excellent conditions for the deep propagation of MW in some segments, which may award it some unique characteristics.

4. Numerical Model and Comparison With Measurements

In Figure 3, we show WRF cross sections from domain d02 along the four HALO flight legs, respectively, for vertical velocity w, temperature T and GW temperature perturbations dT. A horizontal 2D Fast Fourier transform filter was used for the latter. Modes are retained below a 500 km horizontal wavelength, whereby the limit is taken from preliminary campaign results showing the largest significant spatial periodicity observed. The GW
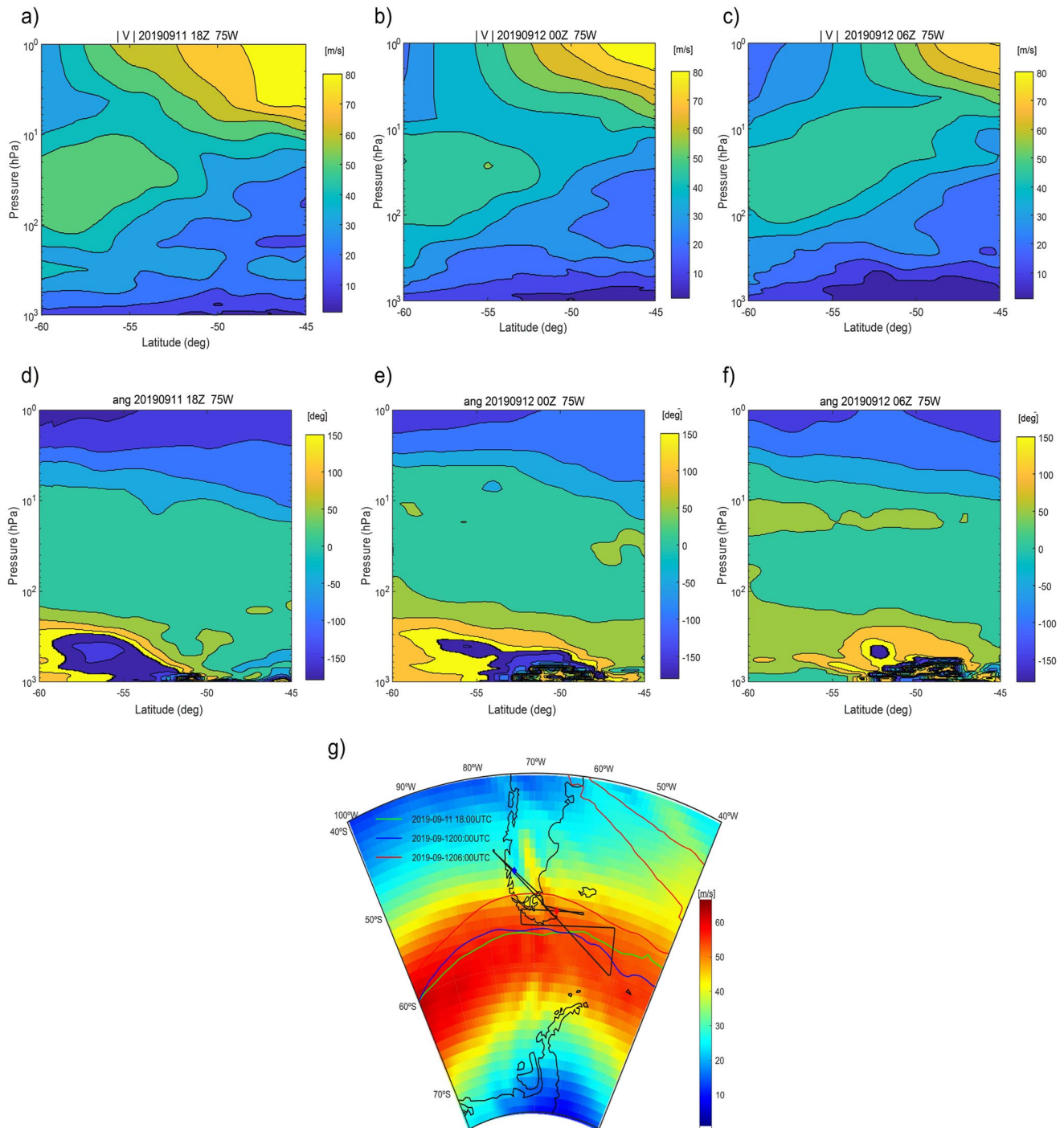
Figure 2. On September 11 at 18 UTC and September 12 at 00 and 06 UTC: (a–c) absolute value of horizontal wind at 75°W, (d–f) angle of horizontal wind at 75°W (measured counterclockwise as from the East direction), (g) magnitude of horizontal wind only on September 12 at 00 UTC and vortex edge location, both quantities at 475K isentropic level.

separation process from the atmospheric background was performed following the description by Kruse and Smith (2015). Distance is reset to 0 at the start of every leg.

Simultaneous BAHAMAS and simulated quantities were compared at given flight times and positions (see the top four panels in Figure 4). Zonal and meridional velocity components u, v and also T and w are represented. Best fits for the former three would roughly approach the ideal case passing through the origin and with slope
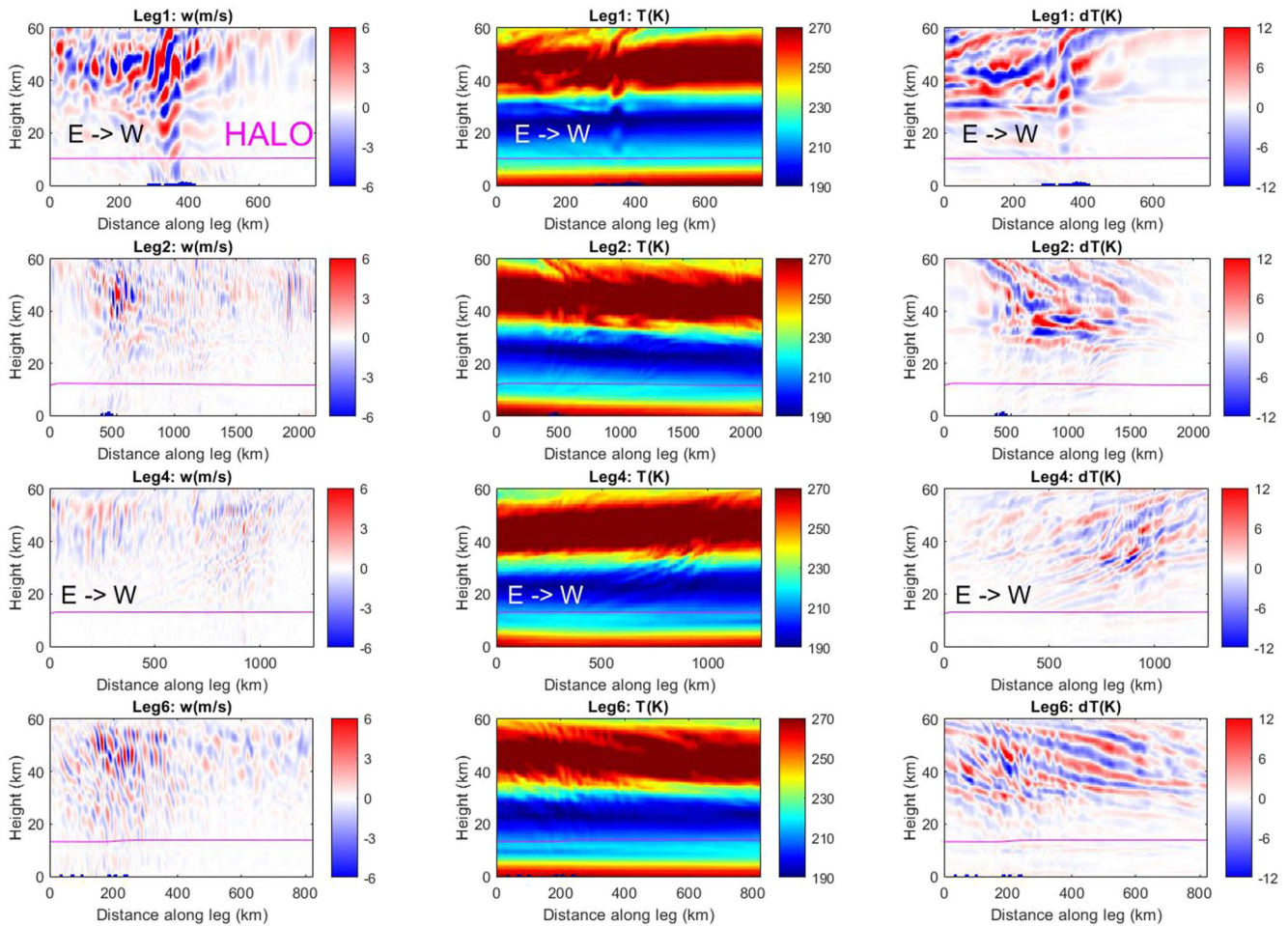
Figure 3. WRF vertical cross sections of w, T, and dT (for horizontal wavelengths shorter than 500 km) along the four studied flight legs as indicated per panel. The aircraft trajectory is also shown in magenta. The dark blue part is a rough representation of topography.

equal to 1. However, w shows deviations from this behavior. In the two lower panels of Figure 4, we focus on this quantity. We represent the probability density function (PDF) for the values from BAHAMAS and WRF along the four legs. The simulated data in all legs show rather a peaked distribution around 0 while the observations exhibit a flatter shape (however, notice that the number of bins for both data sets is the same but not the range of values, so the normalization process is different). Previous works based on observational data acquired during GW campaigns also found significant discrepancies between measured and simulated vertical velocity or associated quantities (e.g., Kruse et al., 2016; Wagner et al., 2017; Wildmann et al., 2021). With the exception of some local agreements, in general w fluctuations seem to occur on quite different scales and amplitudes. In Appendix A, we made in domain d03 higher horizontal resolution (1 km) runs in legs 1 and 2 around Andes to find out if the departure between observed and WRF w is reduced, but no significant improvement was found. We also calculated in Appendix A power spectral densities for w (PSD_w) for WRF and BAHAMAS values in two separate segments (with and without orography) to try to explain the different results from both data sources in the first and second half of leg 6 (see lowest left panel in Figure 5). From that analysis, we could ratify that WRF seems to better reproduce measured w perturbations close to orography than away from it with the largest departures being generally observed at the smallest horizontal scales. Due to these problems, we keep below the use of WRF vertical velocity only for the estimation of the GW drag force and the general identification of MW regions. To distinguish MW and NOGW, we will use both horizontal velocity components of the model to evaluate phase differences between them through the polarization relations and also to calculate vertical wavelengths (see Section 2.3). We should keep in mind that from the polarization relations, we know that w highlights the high-frequency sector of the GW spectrum, whereas du, dv, and dT emphasize the opposite part (e.g., Vadas
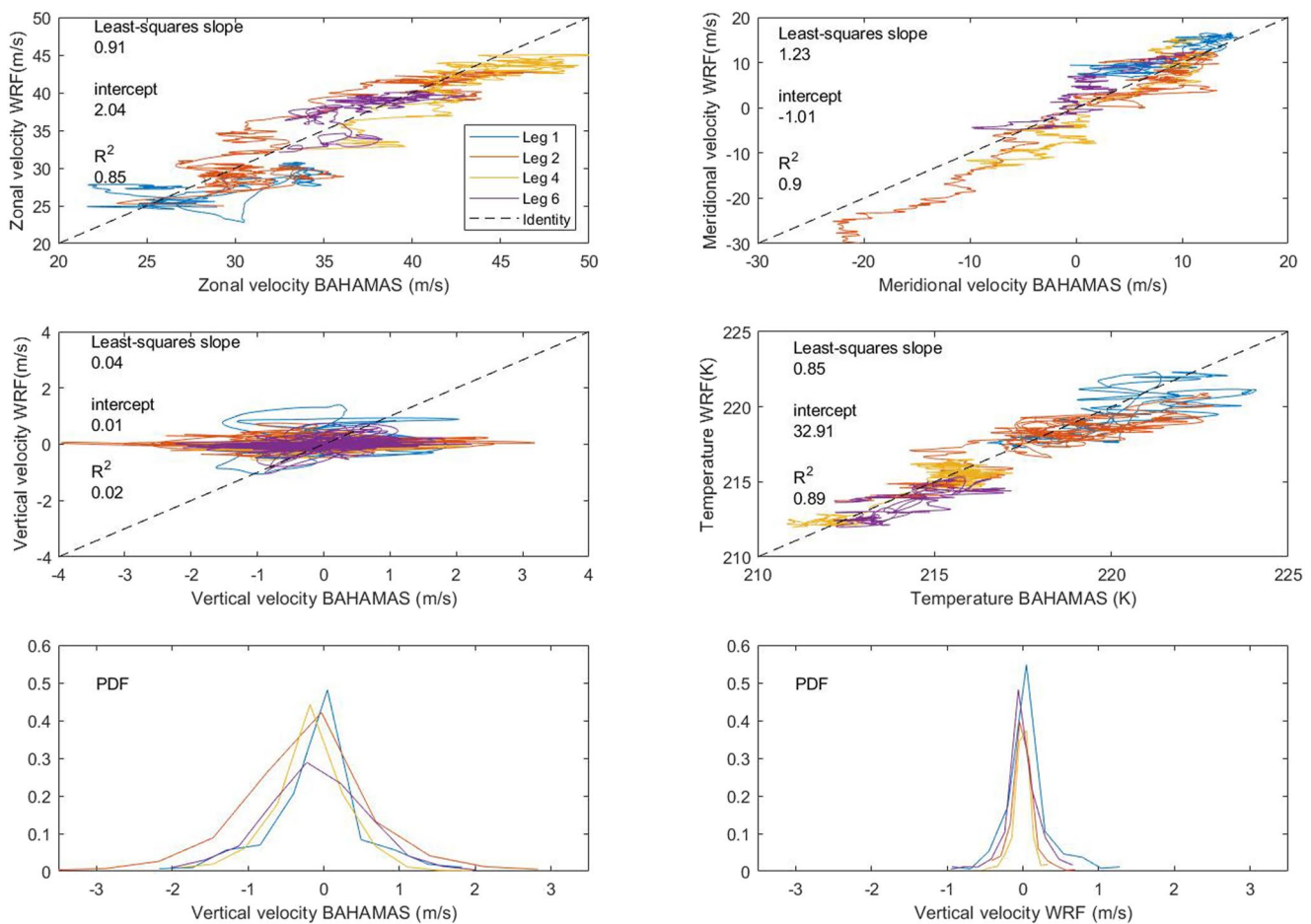
Figure 4. In the four top panels, the relationship between instantaneous values of BAHAMAS and WRF for *u*, *v*, *w*, and *T* is shown. Every point of the lines is associated with the same time and position of the flight. Results for the four studied legs are included. Regression values and the optimal identity line (through the origin and with the slope equal to one) are also shown. The two lower panels show the probability density function for the vertical velocity from BAHAMAS and WRF. Both calculations have the same number of bins but different ranges in obtaining PDF (BAHAMAS *w* extends over a larger interval). The same colors as above are used to represent each leg.

et al., 2018). This implies that only in the ideal case of a single monochromatic mode will the four perturbation variables clearly detect the same GW.

Model and BAHAMAS *w*, *T*, and *dT* in the flight position and time along four segments are shown in Figure 5. There may be in general difficulties with the horizontal wavelength detection even if we neglect the horizontal displacement of non-stationary waves while the onboard instruments sound one full cycle (implicitly assuming that the aircraft speed is much larger than the ground-based horizontal phase speed along the trajectory). If the airplane travels at a given height oblique to the wavefronts, then the real horizontal wavelengths will not coincide with the values detected onboard. These apparent values will be always larger and are related to the deviation of the relative angle on the horizontal plane between trajectory and fronts from 90°. The perpendicular undistorted case may happen just by chance. This kind of difficulty applies to any platform used to measure GW in one horizontal direction (e.g., Alexander et al., 2008; de la Torre & Alexander, 1995; de la Torre et al., 2018). It is not possible to infer the relative orientation between wave fronts and airplane trajectory based only on BAHA-MAS data or any onboard measurements. Therefore, temperature perturbations that are filtered along the HALO path represent onboard apparent modes. The cutoff for Figure 5 was set to 800 km to account for the fact that in general the airplane legs may not be perpendicular to the GW fronts and so apparent horizontal wavelengths may be larger than real ones. The average flight speed was around 850 km/hr and in addition we considered the mean between the WRF resolution when the aircraft moves along meridians or parallels (3 km) and a bisector (4.2 km). Observational data have been averaged over 15 s to make the horizontal resolution of observational
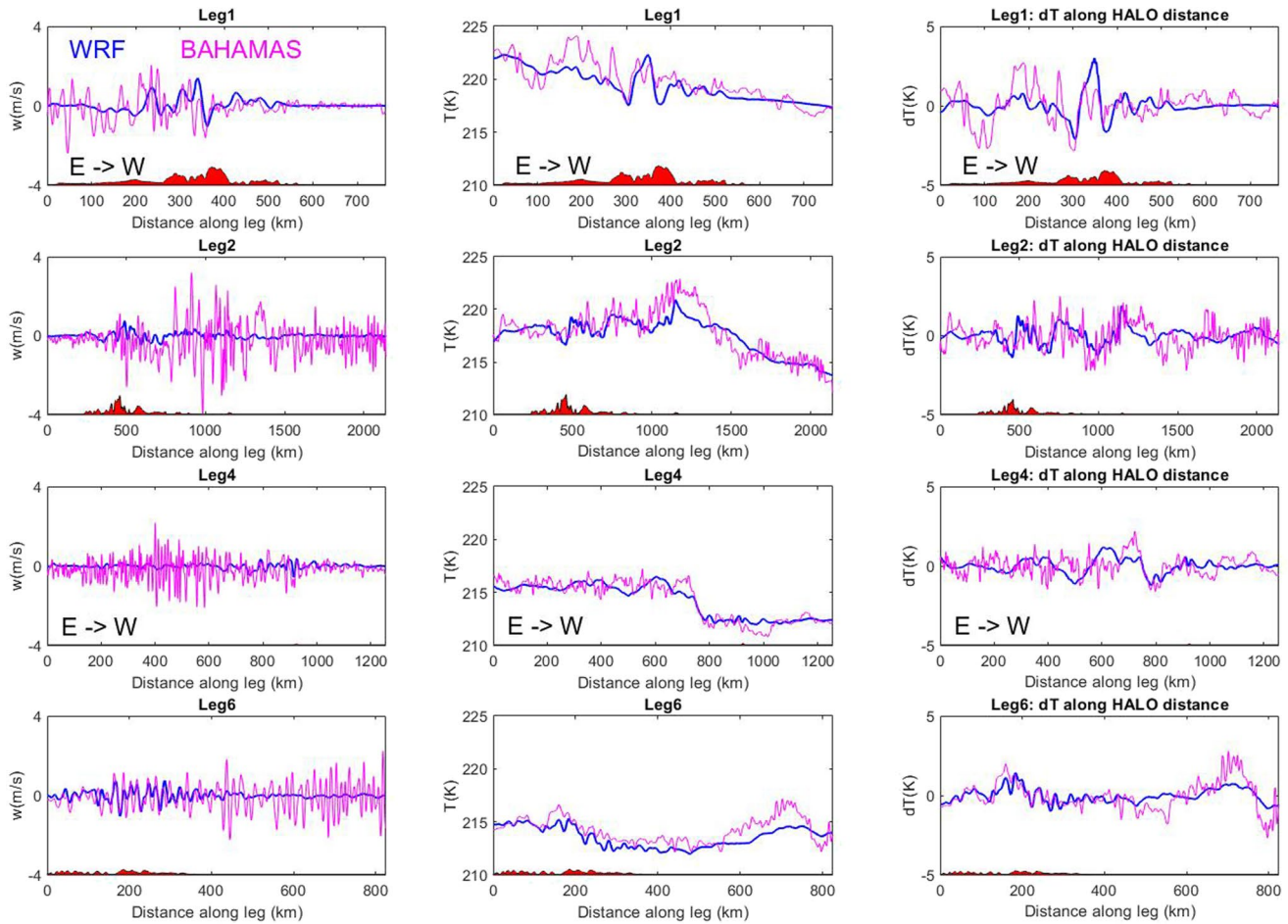
Figure 5. WRF and BAHAMAS *w*, *T*, and *dT* (along the aircraft path) at flight level in the four analyzed segments as indicated in each panel. The lower red part represents topography in an arbitrary scale.

and numerical values comparable. Model results and observations clearly exhibit larger GW activity above and to the East of topography in Figures 3 and 5. The closest match of *w*, *T*, and *dT* between WRF and BAHAMAS may be observed in the first 400 km of leg 6 in coincidence with modest height and slightly sloped topography. For brevity, the horizontal components *u*, *du*, *v*, and *dv* are omitted but the general agreement between WRF and BAHAMAS resembles *T* and *dT*.

Numerical simulations have been horizontally averaged over 30 km to establish comparisons with ALIMA data (the lidar profiles are obtained over 2 min), whereas these values are shown below in the coincident 20–60 km height range. The instrument was affected at some times and altitudes by the presence of polar stratospheric clouds or other issues also impeding the adequate derivation of temperature. Figures 6 and 7 show, respectively, the comparisons of *T* and *dT* filtered between 2 and 20 km of vertical distance (e.g., Ehard et al., 2015; Kaifler et al., 2020). To ensure that the largest vertical wavelengths do not include significant contributions from planetary waves, we plotted the same as Figure 7 but for the perturbations in the spectral range 15–20 km for WRF and ALIMA (not shown) and noticed no horizontal structures of several 100 km with the exception to the West of Andes in leg 1. In this instance, vertical filtering is applied, as from the ALIMA perspective, the relative orientation of wave fronts and aircraft trajectory is unknown. This procedure seems to be physically more adequate if only onboard data are employed as the horizontal wavelength cutoffs chosen along a flight path may be somehow arbitrary without information on the angle between the horizontal wave vector and airplane path. For example, a finite horizontal wavelength can become apparently infinite as detected onboard if the airplane is by chance flying parallel to a constant phase line (e.g., de la Torre et al., 2018). We recall that measured values will always be equal or larger than the real ones. In Figure 6, we notice that although both data sources have very different
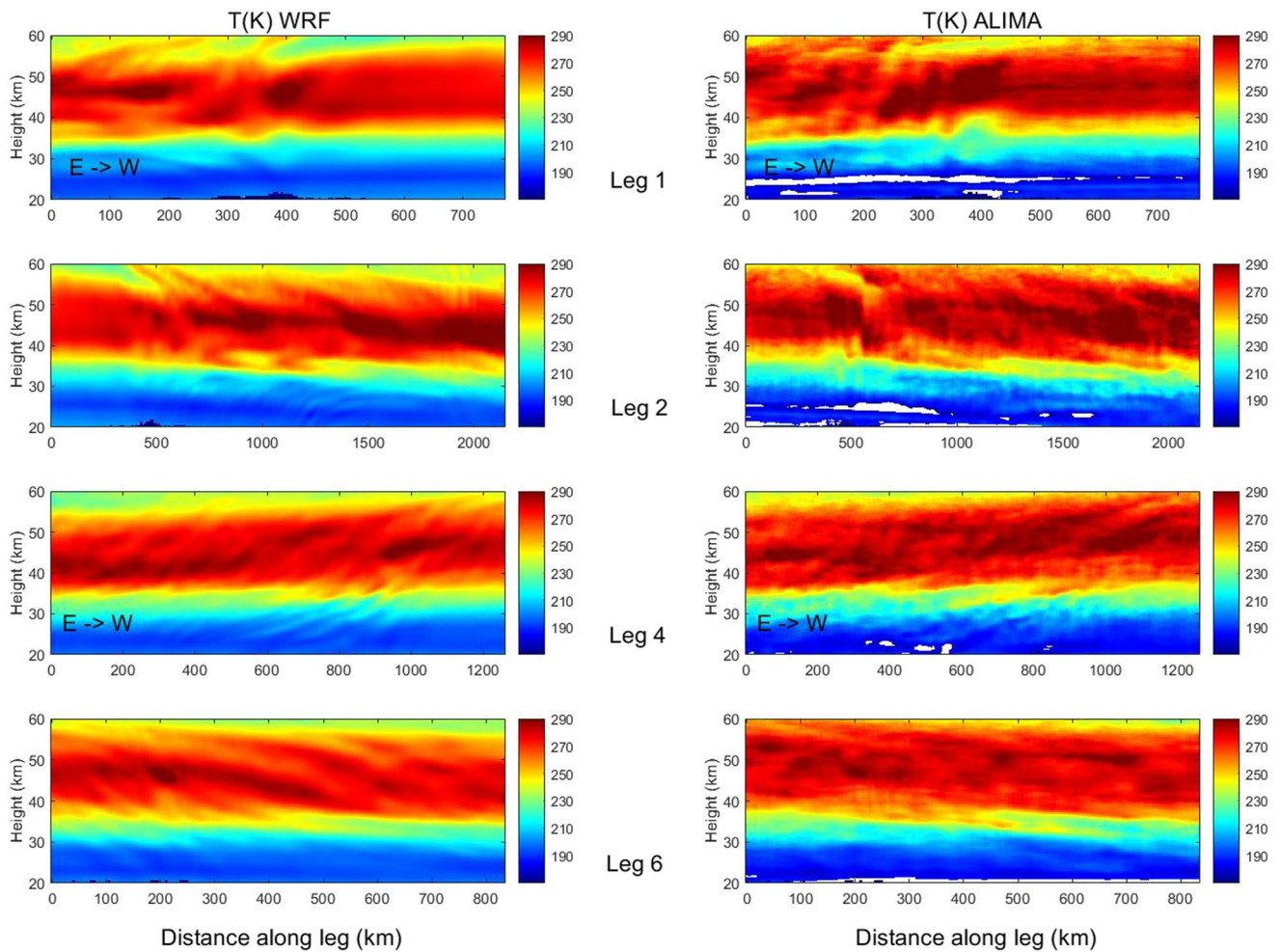
Figure 6. Comparison of vertical cross sections of *T* in the common vertical range of ALIMA and WRF along the four analyzed legs. The dark blue part is a rough representation of topography. White parts in blue sectors correspond to zones where ALIMA cannot measure temperature due to polar stratospheric clouds.

nature they show a coherent picture from the troposphere up to the mesosphere along the four flight legs. The stratopause is observed around 50 km height in both cases. Quantitatively, the observational perturbation amplitudes in Figure 7 differ from WRF solutions but there is a qualitative agreement in order of magnitude and general trends. A significant change in GW behavior is observed around 40–45 km height in some segments and deep propagation in others. We see the MW to the East of Andes in legs 1 and 2 with large amplitudes in *dT*. Legs 4 and 6 also exhibit intense MW, mainly close to topography. In Figure 7, there is a superposition of GW of different scales but it is difficult for the eye to distinguish all of them. ALIMA observations allow to study diverse spectral bands in order to separate different GW modes present during ST08.

5. Results for ST08

5.1. Identification and Analysis of GW Types

We start with some warnings on the complexity of the integration of a large number of data from diverse sources, their processing and physical interpretation. These subjects have already been addressed in previous publications so we do not go into details but we would like to enumerate them as they are a key issue in the use of the campaign results. First, we recall that there is no unique way of separating in the observations the GW from the background, tides, planetary waves, or noise and diverse methods may lead to different results (e.g., Ehard et al., 2015; John & Kumar, 2013). Moreover, it will be noticed that it is not possible to keep the same filtering process for all the data in the present work, as different sources have diverse horizontal and vertical resolutions and may have a
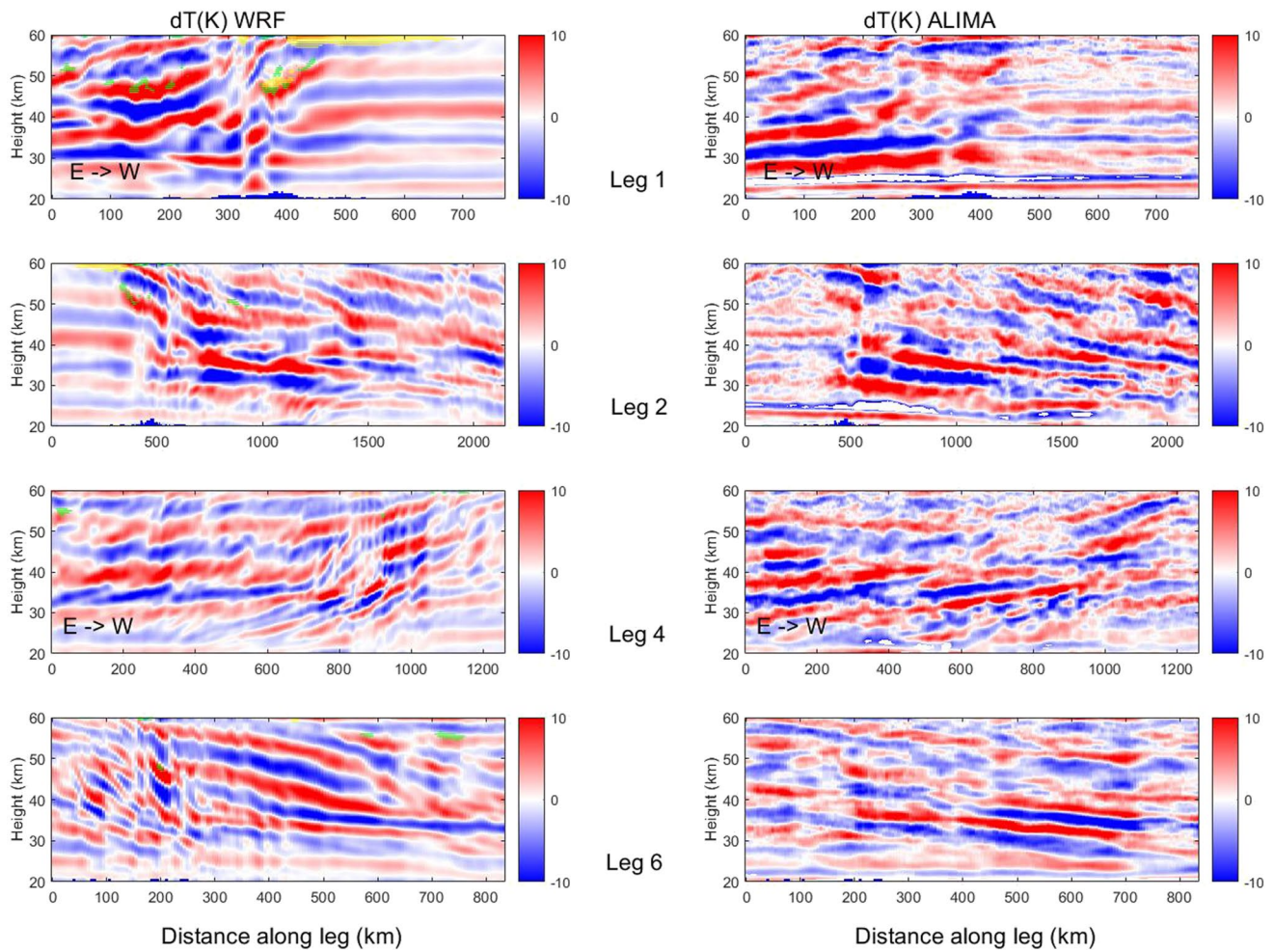
Figure 7. The same as Figure 6 for *dT* vertically filtered between 2 and 20 km. White parts in blue parcels correspond to zones where ALIMA cannot measure temperature due to polar stratospheric clouds. Green sectors correspond to $Ri < 0.25$ and yellow zones to $L^2 < 0$ as calculated from WRF.

one-dimensional, two-dimensional, or three-dimensional perspective. This leads to different minimum or maximum wavelength cutoffs or filtering in the horizontal or the vertical directions for optimization. Second, every instrument may be observing GW in a different spectral range and height and may be operative under different weather conditions (e.g., Preusse et al., 2009). Third, as measurements are not performed simultaneously in the three space dimensions and time, the inferred wavelengths or periods are apparent and usually differ from the real ones (e.g., Alexander & de la Torre, 2010; de la Torre et al., 2018). Careful interpretation is necessary. Fourth, we are submerged in a difficult scenario with no ideal monochromatic waves but rather packets, groups, or superpositions of them or may be there is a dominant mode accompanied by other ones and in addition the linear regime assumption may be fragile. Also, upward and downward secondary components from GW breaking may be pervading a part of the scenario (e.g., Vadas et al., 2018).

In Movies S1 and S2 in supplement, we show the evolution according to WRF domain d02 of *w* and *dT* every 15 min during the flight at 10, 30, and 55 km height (roughly at the tropopause, stratosphere, and mesosphere). In both quantities, it can be seen that the largest GW activity occurred in the first few hours of the flight, mainly above continental Andes and Tierra del Fuego island with amplitudes generally increasing significantly with height. It is predicted by linear theory that the vertical velocity stands out for high intrinsic frequency MW, whereas the horizontal components or temperature may be better suited for the identification of the opposite part of the spectrum (e.g., Gill, 1982). By comparing the videos, it can be seen that the vertical velocity exhibits a more localized pattern above the Andes, confirming that it is a good predictor of MW. It also can be observed that the most significant amplitudes correspond to horizontal wavelengths not much larger than about 100 km. In
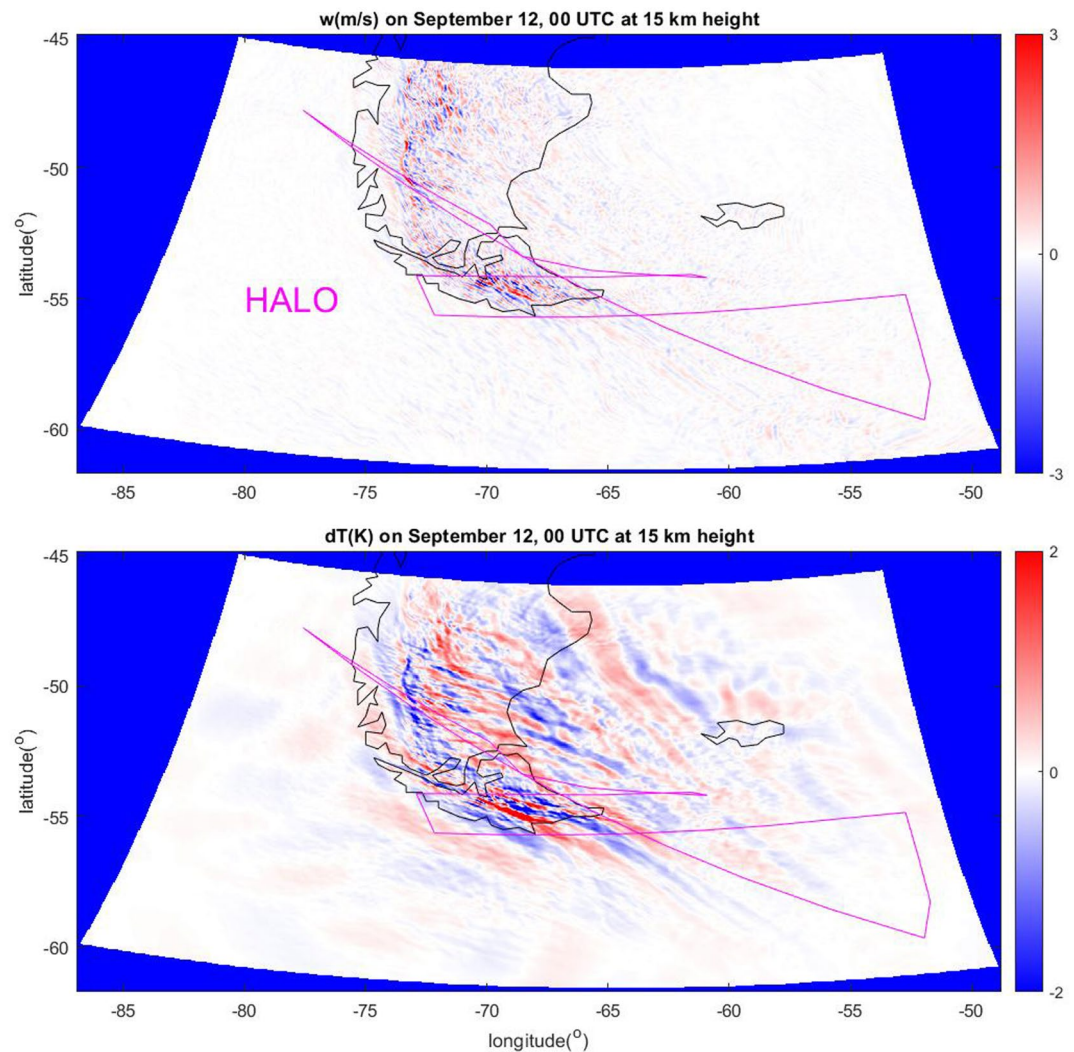
Figure 8. WRF horizontal cross section at 15 km height for *w* and *dT* with a horizontal filter cutoff of 500 km on September 12 at 00 UTC.

Figure 8, we see for WRF domain d02 a horizontal cross-section at 15 km height for *w* and *dT* with a horizontal filter cutoff of 500 km on September 12 at 00 UTC. Signatures of prolongation into the so-called GW belt are clearly seen. The flow over Andes generates the MW that extend downwind and poleward. The two main sources seem to be El Calafate and Tierra del Fuego island areas.

In Figure 9, we show the results of the GW type identification method explained in Section 2.3 and applied to WRF data on September 12 at 00, 02, 04, and 06 UTC. The flight path and the aircraft position at the evaluated times are also exhibited. MW generation at the El Calafate and Tierra del Fuego areas and their advection toward SE are clear during the whole sounding. In addition, NOGW signals are present in the Drake Passage and surrounding area, mainly above oceanic sectors. This fact coincides with many aspects of the rotary spectral study on analysis data during ST08 by de la Torre et al. (2023). The presence of NOGW over the oceans in this region has already been highlighted by Hertzog et al. (2008) and Plougonven et al. (2013). These aspects resemble results from the DEEPWAVE campaign, where MW were mainly found over Tasmania and the South Island and NOGW across the Southern Ocean (Eckermann et al., 2019). The MW over the Southwest at 02 UTC in Figure 9 are of unknown origin or an error of the method. Their approximate vertical localization and wavelength are respectively 20–60 and 17 km whereby the phase difference is about 10°. Taking into account the HALO position over time, it is clear that MW should have been detected by onboard instruments over the four analyzed legs but mainly above the two first ones, whereas NOGW might have been present over the second half of leg 2 and the
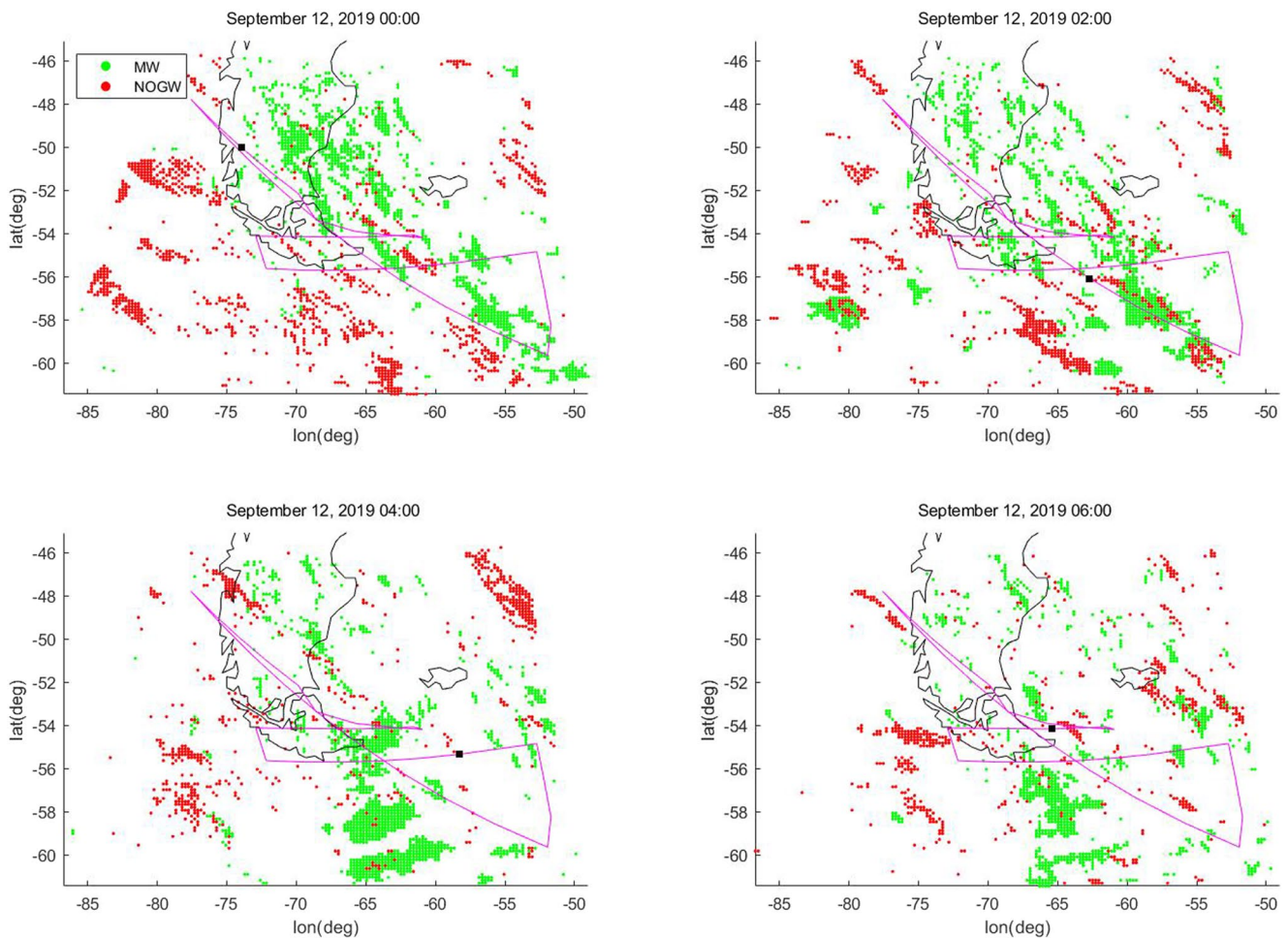
Figure 9. Points in the WRF simulations on September 12 at 00, 02, 04, and 06 UTC where the verification of the polarization relation for both horizontal velocity perturbation components along a vertical column from the ground to 60 km height (coherence above 0.9) determines that it resembles an MW or NOGW. The HALO trajectory (magenta line) and the instantaneous position of the airplane at the time corresponding to each panel (black square) are also shown.

first half of leg 4. In general, the flight rather traversed MW than NOGW. MW sources were apparently dimming by the end of the flight but the wave drift from Andes toward the belt could still be seen (see Movies S1 and S2). Although it is not shown in Figure 9, in each vertical column where the coherence for a mode stayed above 0.9 we determined the altitude of local maximum coherence and the surrounding interval that was still above that cutoff. This allowed us to estimate with the mode vertical wavelength the number of clearly detectable cycles and verify the requirements for MW and NOGW. The figure should not be understood as an exact identification of the location of diverse types of waves but rather in terms of rough areas with likelihood for the presence of them. For example, in Figures 3, 5, 7, and 8, it is clear that when HALO was about the Andes in legs 1 and 2 it crossed strong MW. In Figure 9, just some dots identifying MW are close to those flight positions and times. However, if we look at the overall picture, we will realize that this part of the airplane trajectory is embedded in a clearly (green) MW-dominated region of several 100 km in both cardinal directions. From a general overview of the figure, there is a clear potential for the coexistence in the whole area of MW and NOGW. For example, when analyzing the upper panel on the left of Figure 9, there is a clear dominance of NOGW from the South Pacific through the Drake Passage into partially the Atlantic Ocean and also to the Northeast of the Malvinas Islands. And there is a supremacy of MW in the continent, at the North of Tierra del Fuego and toward the East and Southeast directions. Finally, to the East of this island, both types of GW may likely coexist.

Next, we use BAHAMAS data for comparison with these findings and first focus on wavelet magnitude-squared coherence above 0.7 for w and T for apparent horizontal wavelengths larger than 24 km as seen from the aircraft trajectory. The chosen wavelength lower cutoff is somehow arbitrary with respect to the expected lowest
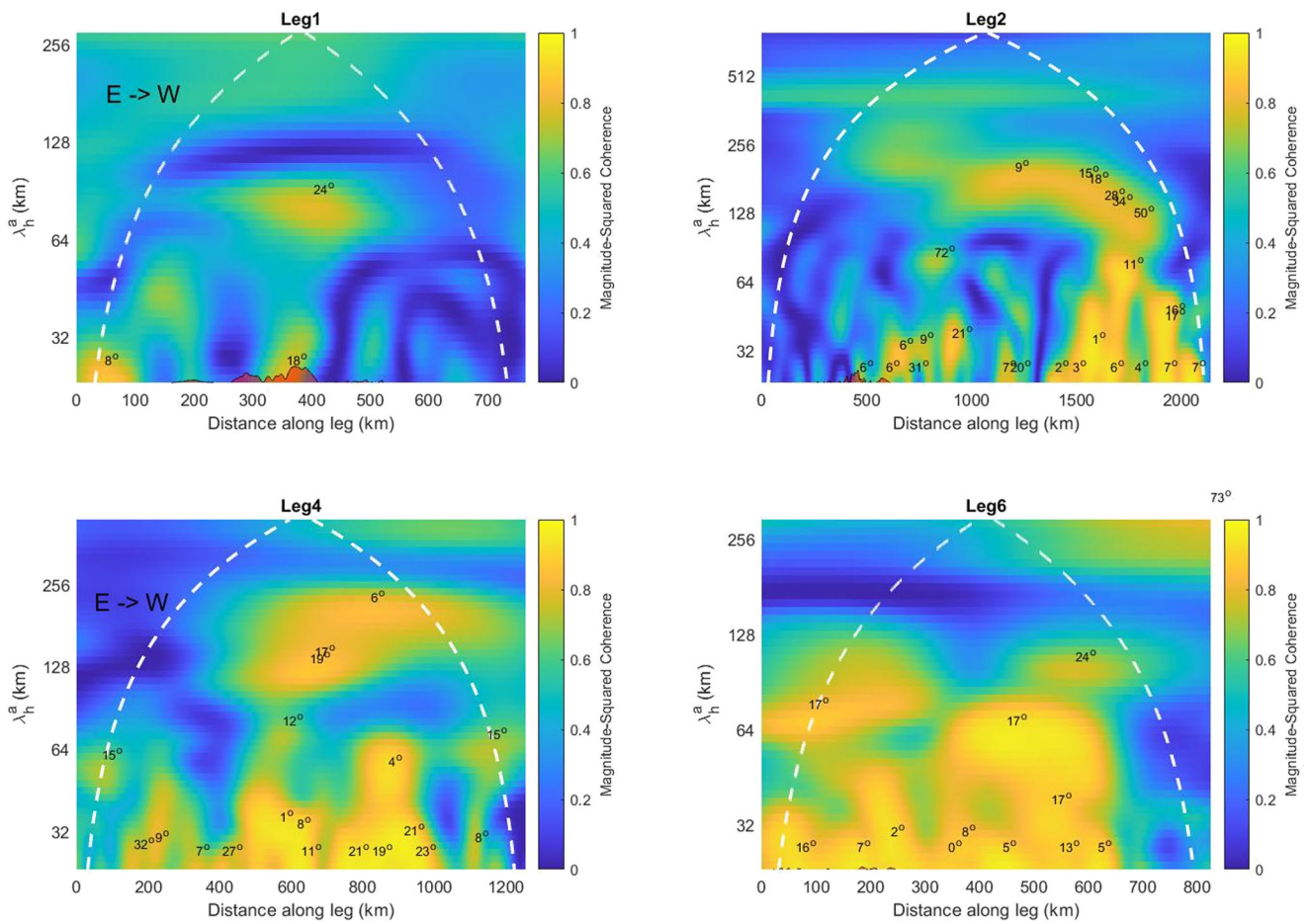
Figure 10. BAHAMAS w and T wavelet magnitude-squared coherence for apparent horizontal wavelengths longer than 24 km as seen from the aircraft trajectory. Where the coherence stays above 0.7, it includes the phase difference departure from 90° (ideal linear non-dissipating GW) at the location of maximal correspondence between both quantities. White dashed lines indicate the limits of the so-called cone of influence where artifacts may start affecting the results. Topography is shown in red and not to scale.

horizontal distance between fronts as seen by the possibly slant path of HALO in the wave field (as explained above horizontal wavelengths measured from the airplane will be larger than real ones). Both magnitudes should be nearly in quadrature for GW unless the vertical wavelength does not suit that it is much smaller than 4π times the density scale height according to the derivation of Equation 3 (Vadas, 2013). In addition, the phase relation holds only if there is no dissipation (Lu et al., 2017; Vadas & Nicolls, 2012). In Figure 10, we show these results, including the phase difference departure from ideal 90° at the location of maximal correspondence between both quantities. Values above 18° may be due to dissipating or large vertical wavelength GW. A variety of GW seems to be present in all legs mostly at shorter apparent horizontal wavelengths. From the coherence analysis of both horizontal velocity perturbations in Figure 11, we notice that the phase difference departure below 18° from ideal linear polarization 0° or 180° indicates that MW may be present along the four studied legs. NOGW may be present in the final part of leg 2 and in the initial section of leg 4 (phase difference above 18° and apparent horizontal wavelength above 100 km). Notice that also with BAHAMAS data NOGW are mainly detected above the ocean. Our 100 km lower limit is somehow arbitrary but reflects the fact that NOGW as short as some MW are less likely to be found (see below Figure 18). Figures 10 and 11 are not fully consistent and therefore need some further discussion on some discrepancies. For example, from Figure 10, one would expect short apparent horizontal wavelength MW in legs 1 and 2 above the mountains. However, they are not observed in Figure 11. One possible cause is that the simple polarization relation in Equation 2 may not hold at some instances because at least one of the assumptions departs from the stated conditions. This might also explain why in Figure 9, the same area is not so full of MW (green) dots. We should recall here that the BAHAMAS results refer exclusively to what becomes detectable at flight altitude.
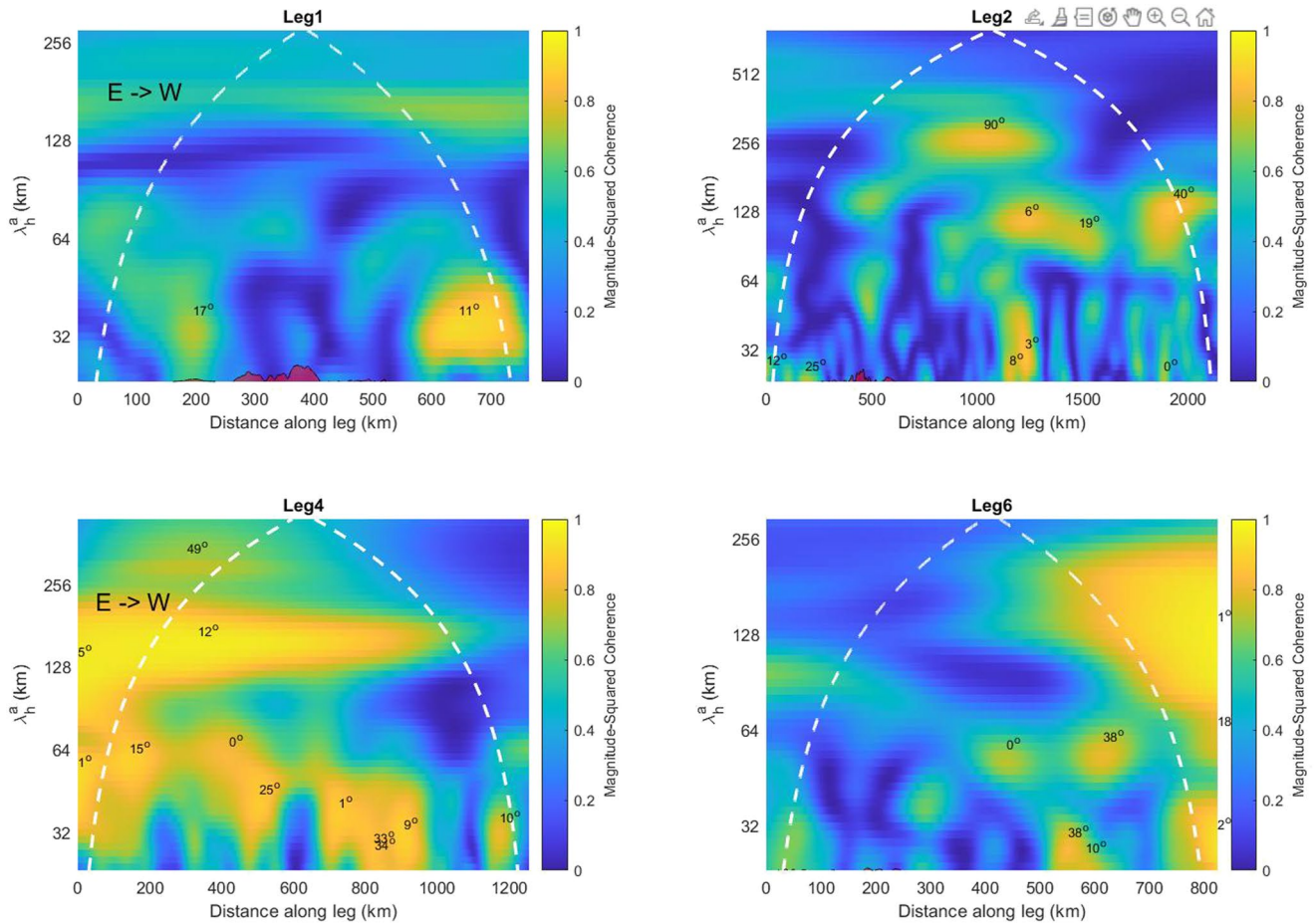
Figure 11. Similar to Figure 10 but for BAHAMAS *u* and *v* and it shows phase difference departure from 0° or 180° (ideal linear MW).

From the results in the two previous paragraphs, we concentrate our search for NOGW in legs 2 and 4 and try to determine some of their general characteristics. We study the coherence of both horizontal velocity perturbation components from WRF along the two flight segments in the vertical columns 0–60 km every 30 km of aircraft displacement. We evaluate the phase difference at the height of maximal coherence and wherever it exceeds 0.7 we determine the altitude interval around that position where it stays above that value. Nearly all possible NOGW detected in terms of phase difference and a minimum of 4 turns stayed within 2.5–5 km vertical wavelength (Figure 12), which justifies our above cutoff of 5 km between NOGW and MW. Regions favorable to the presence of NOGW should be recognized by the repeated exhibition of large columns of high coherence and angles that depart more than 18° from the linear MW ideal condition. In agreement with the above findings, we notice in Figure 12 that the presence of NOGW is corroborated away from sharp topography in leg 2. Along leg 4 (above the ocean), we see the identification of NOGW with a few void intermittencies. This type of wave is essentially visible in WRF above 20 km height. Figure 9 suggests that the whole studied area is a region of encounter between the MW belt and NOGW. Restricting our analysis for that figure to only NOGW and separating them into clockwise and counterclockwise turns with increasing height (respectively downward and upward wave energy flux in the Southern Hemisphere), we notice an overwhelming majority of the latter ones in Figure 13. We may conclude that WRF mainly detects NOGW propagating upwards. Either the numerical model is not able to generate downwards propagating NOGW or the physical source mainly generates them in the opposite direction. Observational data do not lead to firm conclusions regarding the vertical propagation of waves, as BAHAMAS measures the variables along the flight path at a fixed height and ALIMA leads to vertical cross-sections of temperature along the trajectory, so it is not possible to follow the GW vertical evolution at a given geographical position. In agreement with WRF preference of NOGW above the sea, Geldenhuys et al. (2023) detected roughly between 30 and 50 km height with a ray tracer on September 11 at 14 UTC possible evidence of NOGW generated by the jet
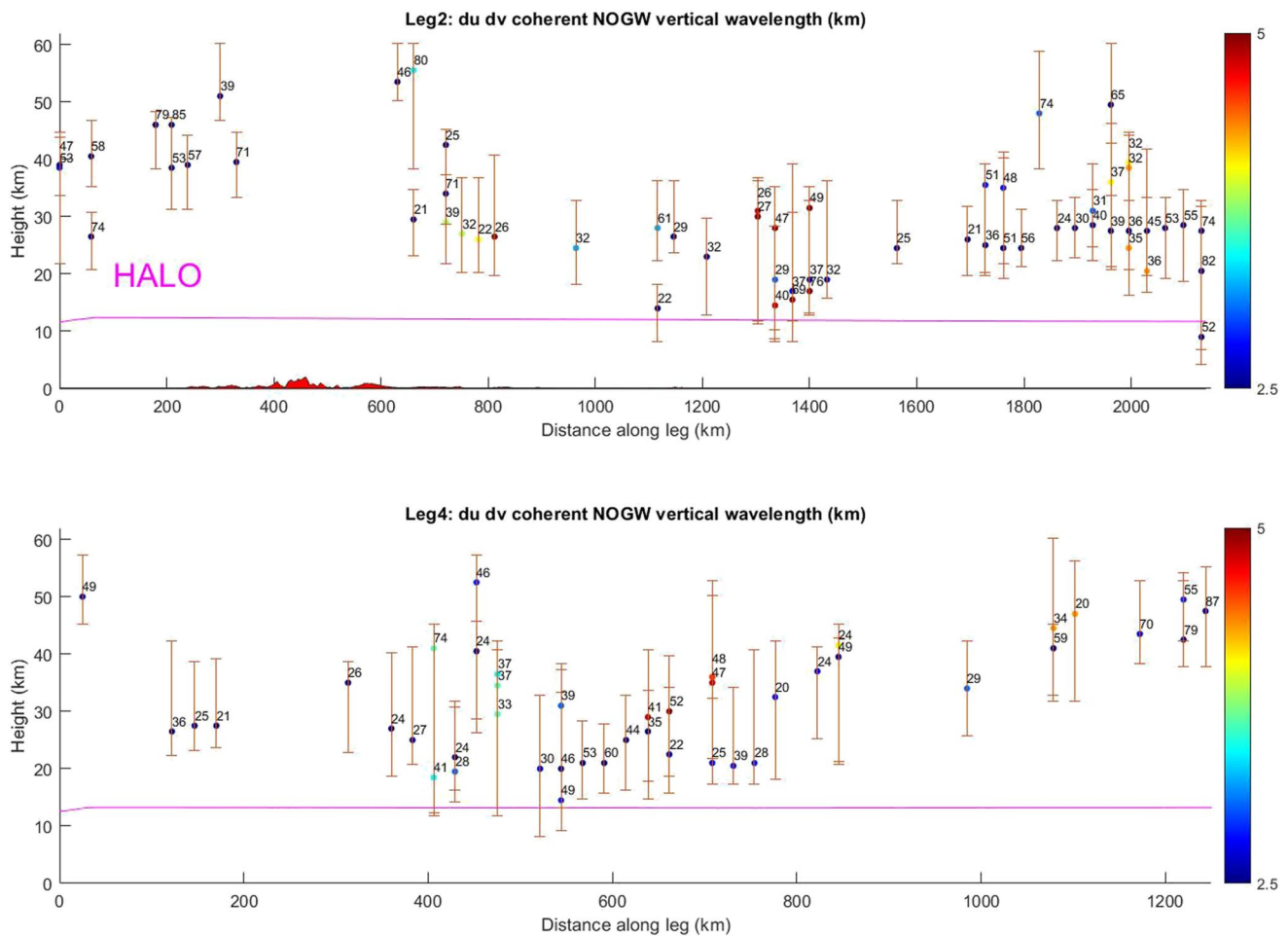
Figure 12. Flight points along segments 2 and 4 where the coherence of both WRF horizontal velocity perturbation components in the vertical columns 0–60 km stays above 0.7. It is evaluated every 30 km of aircraft trajectory. The colors identify the optimal vertical wavelength. Numbers indicate the phase difference at the height of maximal relationship and the vertical intervals show where the coherence stays above 0.7. A minimum of 4 turns is required for the identification of NOGW. Topography is also shown in the lower part of the panels.

over the Pacific Ocean upwind of the Andes. It is also remarkable that Vadas and Becker (2018) observed with numerical modeling a significant presence of inertia-GW over the circumpolar ocean surrounding Antarctica during wintertime.

To further analyze NOGW in the region, we study them in the Drake Passage area where according to Figure 9 they exhibit a significant presence at least in the initial hours of September 12. In Figure 14, we show the perturbed horizontal velocity components around the flight area at 25 km height on September 12, 02 UTC according to WRF. Although vertical wavelengths of the three-dimensional profiles have been filtered between 2.5 and 5 km, it is clear that it is not possible to fully eliminate some fingerprints of MW that possess short horizontal scales (the alternating fringes): in the Southeast zone of the panels, a region with homogeneous sectors (large horizontal scale NOGW) but also with weak fronts (presumably traces of MW after filtering) may be seen. In Figure 15, we observe the NOGW in this area with zonal and meridional vertical cross sections of both horizontal velocity perturbations (in the position of the cross in the upper panel of Figure 14). Every ° represents here in latitude and longitude, respectively, about 111 and 60 km. Fronts are more clearly visible above 25 km height. Vertical wavelengths generally stay around 5 km. In Figure 16, we see the rotation of the horizontal perturbation vector in the position of the asterisk in the upper panel of Figure 14 (this point was chosen for the clean rotation as compared to other ones in the Drake Passage). About six full cycles happen in the height interval from 26 to 56 km (vertical wavelength around 5 km). The ellipse orientation seems to show that the wave vector direction is mainly West to East (with an ambiguity of 180°). The eccentricity in general is not larger than 1/2. There is
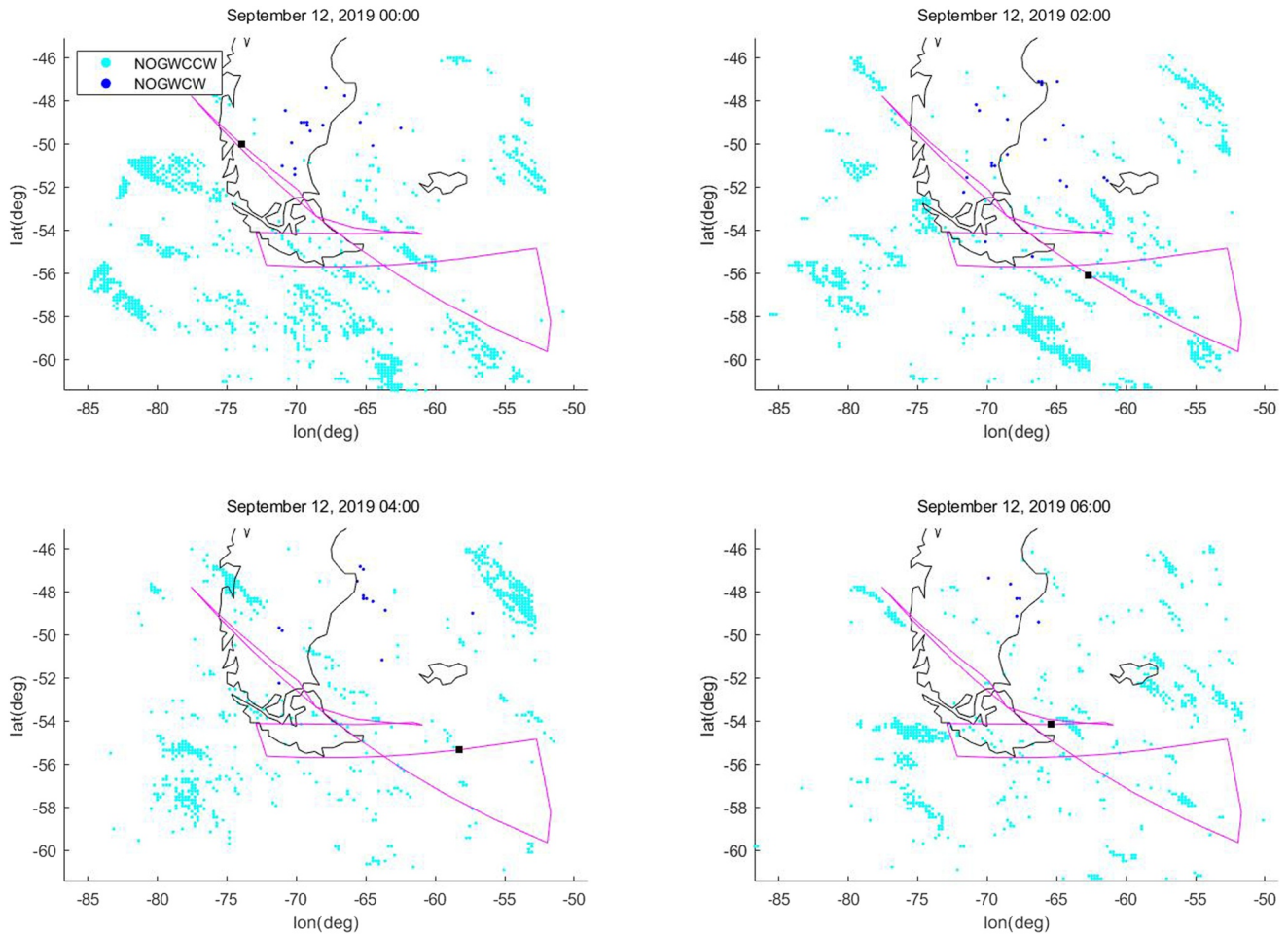
Figure 13. Points in the WRF simulations on September 12 at 00, 02, 04, and 06 UTC where the verification of the polarization relation for both horizontal velocity perturbation components along a vertical column (coherence above 0.9) determines that it resembles a clockwise (CW) or counterclockwise (CCW) NOGW. The HALO trajectory (magenta line) and the instantaneous position (black square) are also shown.

a slight change with height (i.e., of the intrinsic wave frequency). This may be explained by the fact that GW propagate simultaneously in the horizontal and vertical directions so when we look straight upwards we may not see the same wave along the whole vertical line. Or we might have no monochromatic mode but rather a packet. In the complementary work (de la Torre et al., 2023), it is shown through a spectral analysis in the flight area and time of ST08 that monochromatic waves are hardly found and rather bands around one or two dominant modes are detected.

It is noteworthy that most NOGW observed by WRF (Figures 12, 15, and 16) are located above the lower stratosphere (see Figure 3), propagating upwards and usually around regions dominated by MW. We therefore evaluate the Richardson number (Ri) values in order to probe another possible NOGW source like MW breaking due to convective or dynamic instability by respectively verifying values below 0.25. It is calculated as

$$\mathrm{Ri} = \frac{N^2}{(dU/dz)^2}$$

where $(dU/dz)^2$ refers to the squared vertical gradient of both horizontal velocity components and $N^2 = g/\theta \, \partial\theta/\partial z$ with θ potential temperature. The so-called wave-modulated or local Richardson number (Nappo, 2012) has been calculated here. We therefore set the filter cutoffs selectively to the vertical profiles above every grid point as now explained. When calculating N^2, scales shorter than 20 km are removed from θ so that it represents only the background. For the vertical derivative $\partial\theta/\partial z$ the scales smaller than 5 km are eliminated, so the gradient is associated to the background with MW perturbations. Finally, to complete the calculation of Ri, the wavelengths shorter than
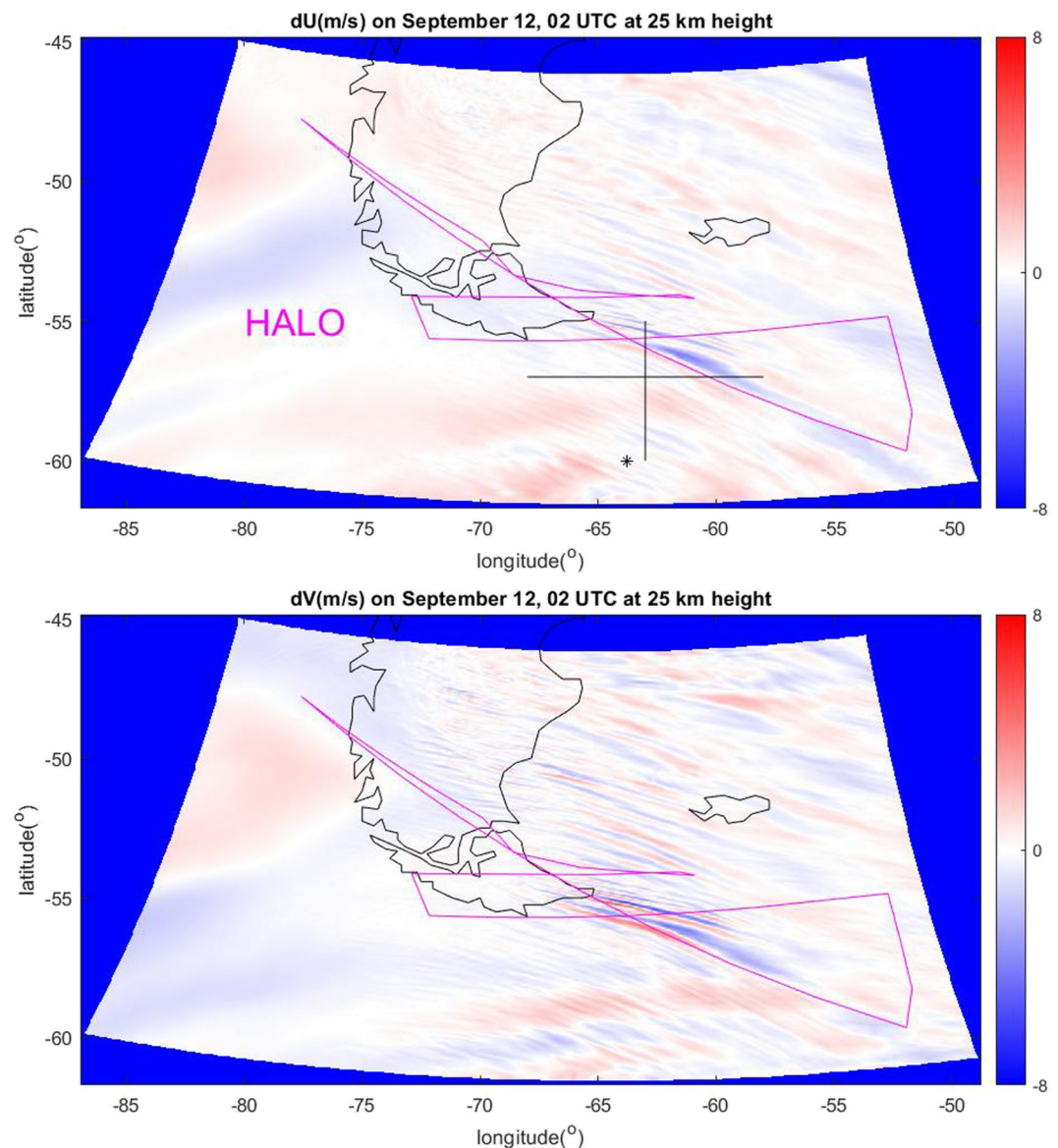
Figure 14. Horizontal cross sections for both WRF horizontal velocity perturbations vertically filtered between 2 and 5 km at 25 km height on September 12, 02 UTC.

5 km become removed for the horizontal wind components. A few notable zones emerge along the four segments from the condition $Ri < 0.25$ and are shown in green in Figure 7. They are mainly located over Andes in leg 1 and always above 45 km. The marked areas are in agreement with the above description of ALIMA and WRF data showing a notable change in GW behavior in the upper stratosphere in some segments. The features may be interpreted as GW breaking or attenuation and secondary waves around that height (Kogure et al., 2020; Vadas et al., 2018). However, considering this altitude, the phenomenon cannot be the source of all the NOGW that are mainly above the oceans. Then, there is a chance that some of these waves are the leftovers from the cold front mentioned above as it agrees with the WRF result of nearly all those waves propagating upwards.

We also use the Scorer parameter (Scorer, 1949)

$$L^2 = \frac{N^2}{U^2} - \frac{1}{U}\frac{d^2U}{dz^2}$$

to distinguish areas where MW, if they are present, may be evanescent, trapped or vertically propagating. According to the parameter definition, N and U are the corresponding background profiles. The calculations lead to permitted hori-
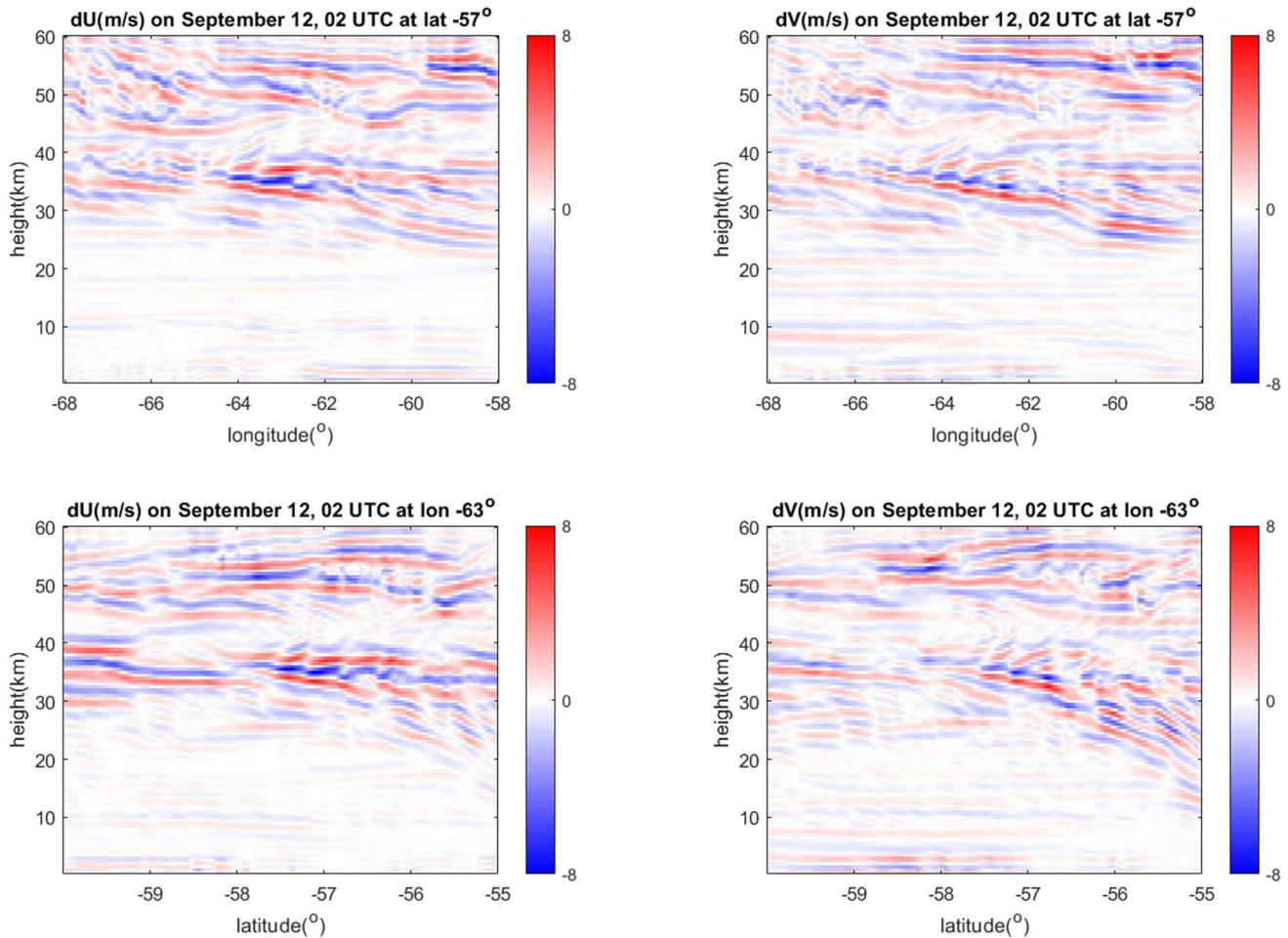
Figure 15. Vertical cross sections as located in the black cross in the upper panel of Figure 14 for both WRF horizontal velocity perturbations vertically filtered between 2.5 and 5 km on September 12, 02 UTC.

zontal wavelengths above a few km except in some areas represented as yellow in Figure 7, where the Scorer parameter becomes negative and no MW could propagate conservatively upwards. This is contrary to a sometimes made assumption that the first term in the Scorer parameter definition may be dominant. At least from the present simulations, this may not be the true behavior in some parts of the mesosphere. This situation seems to occur over the mountains around 50 km height in the first two legs (with some amplitude attenuation above) and around 60 km in the last two ones.

5.2. GW Energy and Momentum Flux and Drag

We now calculate GW energy and zonal and meridional momentum fluxes (EF, MF_x, MF_y) at flight level as indicated by Smith et al. (2008, 2016) and compare between results obtained with BAHAMAS and WRF data. Averages per segment are calculated as

$$MF_x = \frac{\overline{\rho}}{S} \int du\,dw\,dS$$

$$MF_y = \frac{\overline{\rho}}{S} \int dv\,dw\,dS$$

$$EF = \frac{1}{S} \int dp\,dw\,dS$$

from GW perturbations in the three components of velocity du, dv, dw and pressure dp, $\overline{\rho}$ is the average density over the segment and S and dS are its length and a differential displacement over it. According to Eliassen and Palm (1960) for linear, steady, small-amplitude, non-dissipative MW
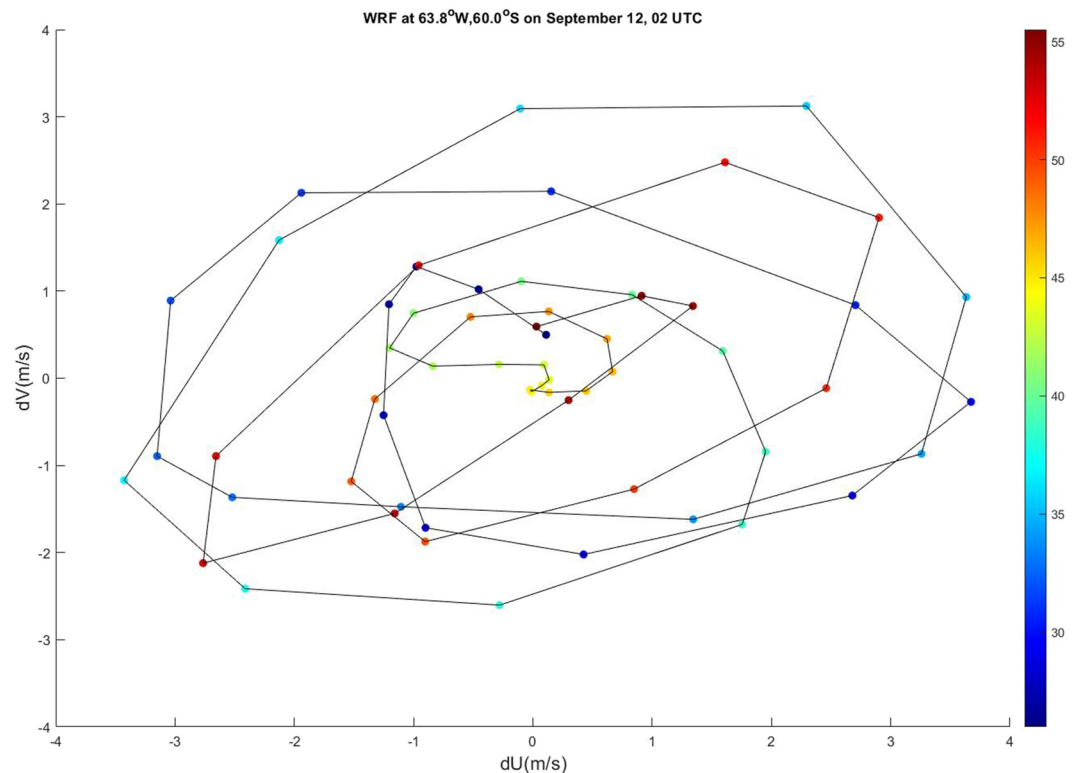
Figure 16. Elliptical rotation with height of the WRF horizontal velocity perturbation vector in the black asterisk shown in the upper panel of Figure 14 on September 12, 02 UTC.

$$-EF = \overline{u}MF_x + \overline{v}MF_y$$

with zonal and meridional velocities $\overline{u}$ and $\overline{v}$ averaged per leg. Perturbations are obtained by removing any mean and linear trend along the segment. A hydrostatic correction is previously applied to pressure. Departures from the above relation may indicate deviations from the cited assumptions. In our case with the exception of leg 1, we cannot claim that most observed GW are MW. In addition, with respect to above results, we cannot assume that all perturbations are linear, steady, small, and non-dissipative. However, the relation is here roughly obeyed. Values are within usual ranges and they approximately agree with calculations from Dörnbrack et al. (2022), who analyzed 357 segments of the whole SOUTHTRAC campaign. Their legs 1, 2, 4, and 5 are similar but not coincident with our 1, 2, 4, and 6. In Table 1, we compare our values obtained from BAHAMAS and WRF. Notice that almost all values are positive, which could imply upward propagating MW carrying negative momentum. However, the results stem from path integrals so they could also just show that in general the upward exceed the downward momentum fluxes. We mention that when we filtered out from BAHAMAS any fluctuations over an interval smaller than 150 consecutive data (15 s, which is roughly equivalent to a HALO distance of 3 km) to mimic the WRF horizontal resolution, then the results did not change significantly so we omit them here. Leg 4 exhibits consolidated differences between EF and $-(\overline{u}MF_x + \overline{v}MF_y)$ within WRF and BAHAMAS data and this could be attributed that it is fully above ocean and according to our above results more susceptible to the presence of NOGW. The only negative value (leg 2 with BAHAMAS data) could be attributed to its long raid over the ocean (where a significant amount of NOGW may be present according to Figure 9). Another possibility is a contribution from downwards propagating secondary waves originated in MW breaking. This large negative value in the same leg was also found by Dörnbrack et al. (2022). However, $EF < 0$ has previously

Table 1
Vertical Gravity Wave Energy Flux EF for Legs 1, 2, 4, and 6 Calculated Directly and Through the Momentum Flux With BAHAMAS and WRF Data

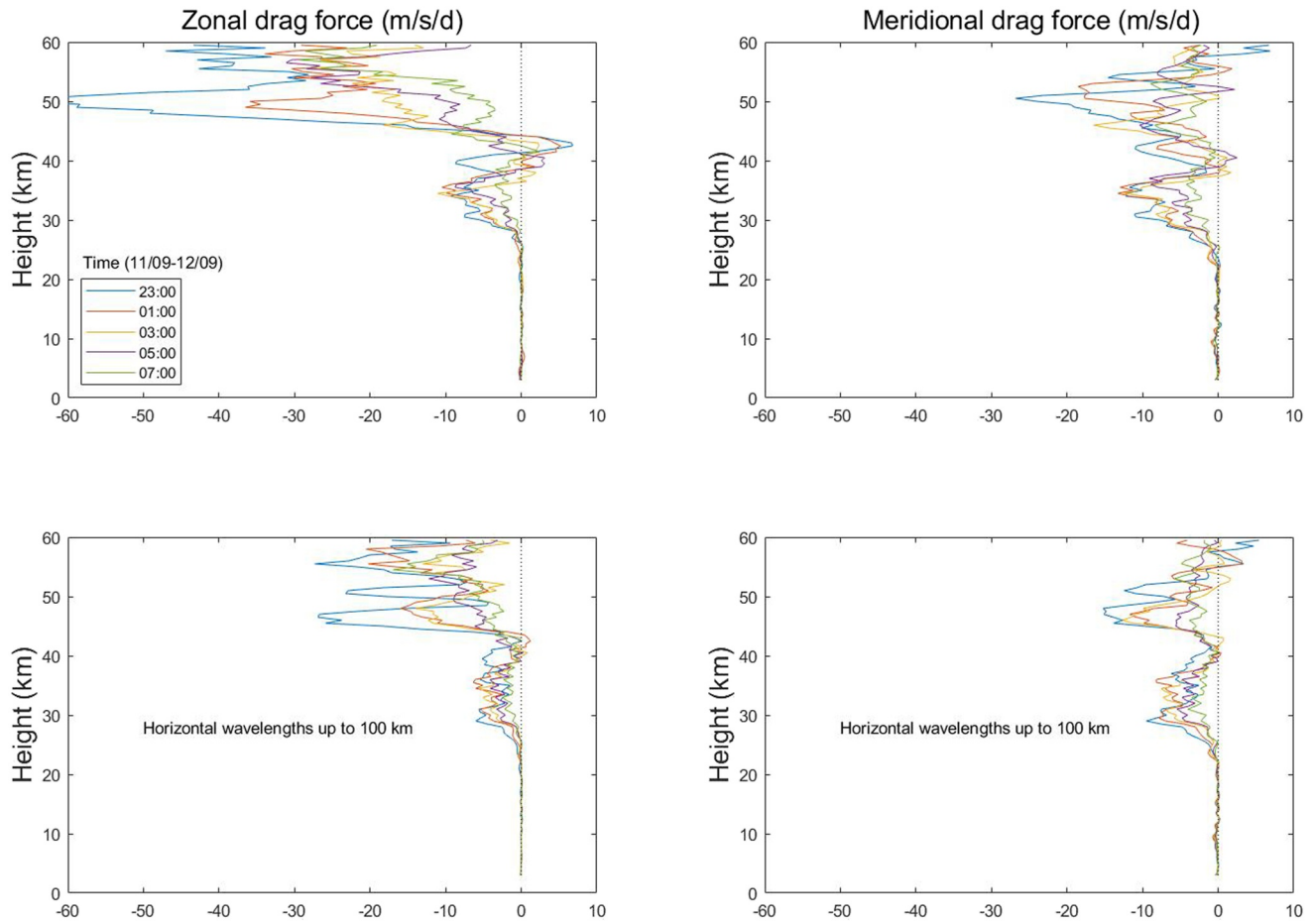|	BAHAMAS		WRF	
Legs	$-(\overline{u}MF_x + \overline{v}MF_y)/$ (W m^{-2})	$EF/$(W m^{-2})	$-(\overline{u}MF_x + \overline{v}MF_y)/$ (W m^{-2})	$EF/$(W m^{-2})
1	2.0	1.8	0.5	0.8
2	−1.2	1.5	0.7	0.4
4	0.4	1.6	0.5	1.1
6	1.2	1.3	0.4	0.2

Figure 17. The zonal and meridional drag components as obtained from WRF simulations every 2 hr from September 11, 23 UTC to September 12, 07 UTC in the rectangle defined by 77°W, 63°W, 60°S, and 45°S. The two top and two lower panels correspond, respectively, to the contribution of horizontal wavelengths shorter than 500 and 100 km.

also been obtained in some MW-dominated areas with no unique explanation (e.g., Dörnbrack et al., 2022; Smith et al., 2008; Wagner et al., 2017).

GW momentum flux was calculated from the WRF simulation in a rectangle containing the whole flight area and the corresponding drag zonal and meridional components were obtained for horizontal wavelengths shorter than 500 km (Figure 17), as explained by Kruse et al. (2016). The two drag projections had comparable negative components but the zonal contribution was generally larger. There is a one order of magnitude increase about 25 km height and a maximum at 50 km altitude. GW horizontal refraction caused by wind gradient may be one of the contributors to the drag due to the variations it produces on momentum flux (Geldenhuys et al., 2023). In coincidence with the GW activity exhibited by both videos, the largest intensity occurs at the beginning of the flight and thereafter there is a weakening evolution. The drag values and profiles are similar to those calculated by other means in this GW hotspot area (Kaifler et al., 2020). By neglecting the contribution from GW close to the inertial frequency as the factor $F = 1 - f^2/\hat{\omega}^2$ tends to 0 for those waves (Fritts & Alexander, 2003) and assuming a linear regime we obtained the zonal drag as

$$-\frac{1}{\bar{\rho}}\frac{d}{dz}\left(\bar{\rho}\overline{du\,dw}\right) \tag{4}$$

where $\bar{\rho}$ here represents the background density, z the altitude, $\overline{du\,dw}$ the Reynolds stress averaged over at least one typical horizontal wavelength distance or area (a similar expression holds for the meridional drag). We should assess the uncertainty introduced in the calculation by assigning to F a value of 1 also to the GW that stay away from the high intrinsic frequency regime, at least at altitudes where the drag is large (above 25 km).
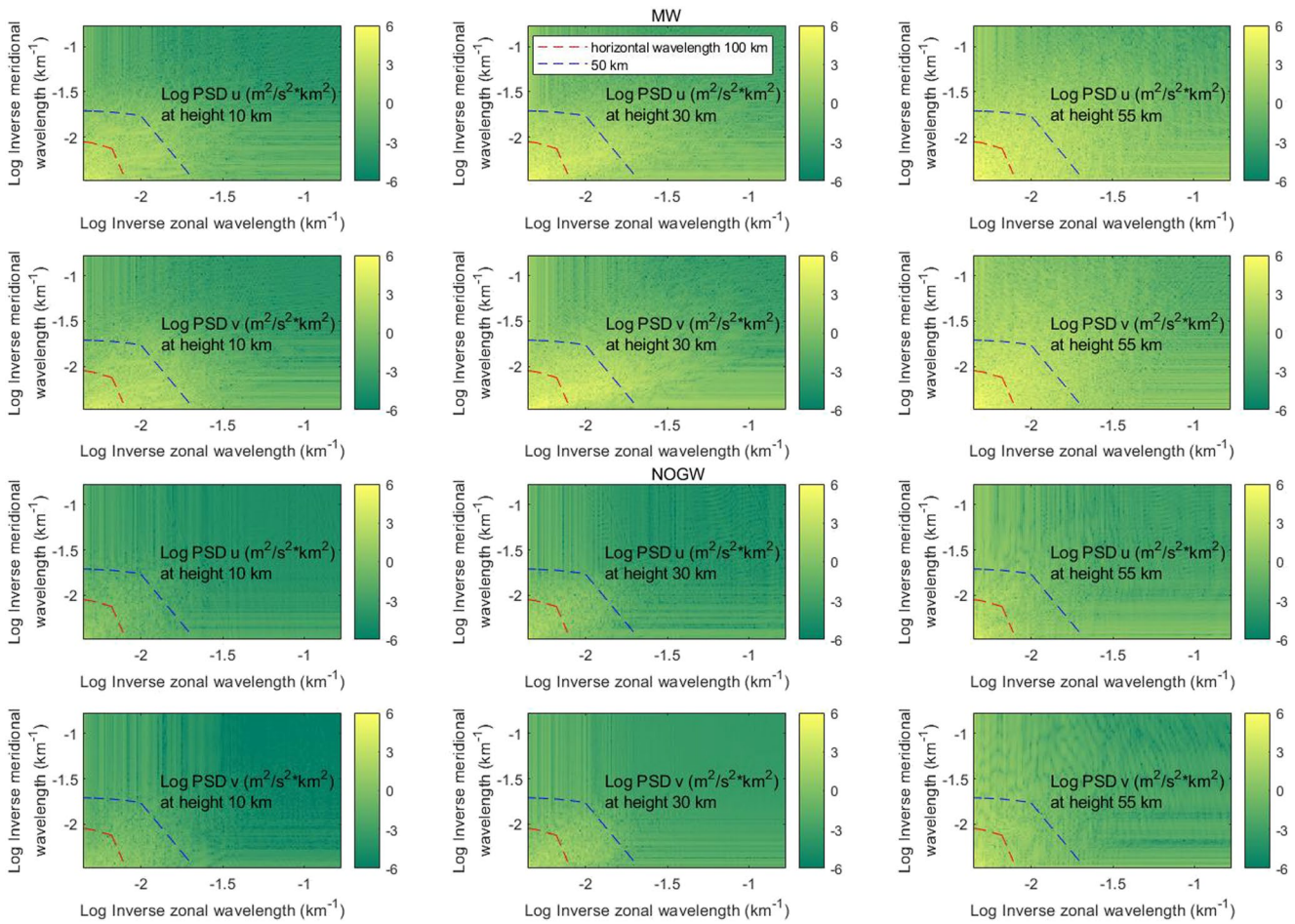
Figure 18. Two-dimensional power spectral density for both horizontal velocity components at three different heights on September 12, 00 UTC. The dashed lines show two total horizontal wavelength values (50 and 100 km) in terms of the zonal and meridional components. Lower panels refer to a rectangular zone dominated by NOGW (longitude −85° to −75° and latitude −50° to −58°) and higher panels correspond to a region governed by MW (longitude −75° to −65° and latitude −55° to −47°).

From Figure 16, we may derive representative information. The eccentricity of the ellipse indicates the ratio of wave intrinsic frequency to Coriolis parameter $f/\hat{\omega}$. Above 25 km, the value is about 1/2 or even lower. This implies that the contributions from NOGW to the total drag could be at most 25% lower than when we use an F value of 1.

The strongest drag components may be observed in the upper panels of Figure 17 around the upper stratosphere and stratopause, and it coincides with the altitudes mentioned by McLandress et al. (2012) for the missing drag. Above 40 km height, there is a trend toward a sign reversal of the force. In the lower panels of the figure, we recalculate the drag but only for horizontal wavelengths smaller than 100 km. They explain a very large portion of the total drag above 25 km height, mainly close to the stratopause. Figure 15 gives an idea of ranges of NOGW horizontal wavelengths. A sharp spectral separation from MW may in general not be possible. In Figure 18, we show the power spectral density for both horizontal velocity components at three different heights for respectively rectangular regions dominated by MW (longitude −75° to −65° and latitude −55° to −47°) and NOGW (longitude −85° to −75° and latitude −50° to −58°) according to Figure 9 on September 12, 00 UTC. It may be noticed that in general MW dominate the spectrum (keep in mind that PSD scales are logarithmic) at total horizontal wavelengths lower than 100 km. We may therefore evaluate that most of the drag from this spectral range stems from MW, which is roughly half the total opposing force at those heights.

From the above comments on the discrepancy of w between WRF and BAHAMAS at flight level, it is clear that the current drag results are disputable. However, we remark the notable similarity of our results with the drag
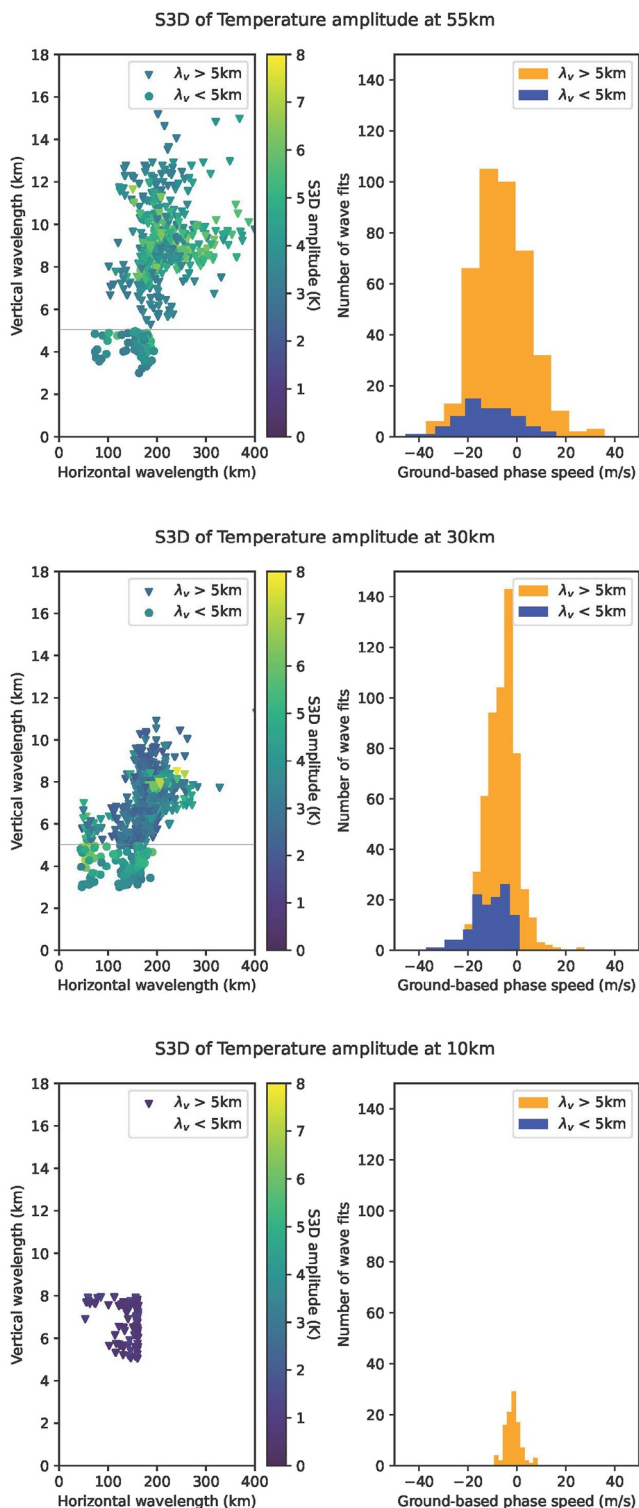
Figure 19. On the left panels, perturbation temperature amplitudes found with S3D in WRF domain d02 on September 12 at 03 UTC at heights 10, 30, and 55 km are shown in terms of horizontal and vertical wavelengths. On the right panels we exhibit histograms of cases per horizontal ground-based phase speed. Results are separated according to vertical wavelengths (λ_v) larger or smaller than 5 km (a priori MW or NOGW). A gray horizontal line in both top panels on the left shows the borderline between both populations.

profiles from Kaifler et al. (2020) obtained with a lidar in the same region and season of the year.

6. Discussion and Conclusions

From the numerical simulations, we may infer that the most intense GW occurred before and at early stages of flight ST08. They were located above Andes with amplitudes increasing significantly with height. The cleanest GW vertical patterns in the WRF mesoscale simulations may be found in leg 1 above Andes. The two main local sources of MW from the numerical simulations are El Calafate and Tierra del Fuego. These waves extend southeastwards toward the so-called GW belt. WRF and BAHAMAS both indicate the presence of significant NOGW above the ocean but no clear source could be identified. This configuration of MW mainly above topography and NOGW above the ocean has also been observed in another hotspot during the DEEPWAVE campaign. The classification of waves into MW or NOGW has been done using WRF and BAHAMAS data with polarization relations and by verifying links between wave energy and momentum fluxes. According to Figure 9, flight ST08 mainly probed MW rather than NOGW. The calculation of Richardson and Scorer numbers shows some localized places in the four studied legs, mainly above the mountains, where GW in the upper stratosphere or lower mesosphere underwent instability.

Some results of the rotary spectral study on analysis data by de la Torre et al. (2023) and some outcomes of our work based on mesoscale simulations in the region and time of flight ST08 should be highlighted together. Their calculated upward GW energy flux is generally largest around the mountain zones and in some oceanic areas. This means that from a statistical point of view most of those propagating GW were generated in the lower atmosphere. They also found that above the lower stratosphere, the wave energy fluxes were much larger than below. This fact implies that there may have been some GW sources around the middle stratosphere. Throughout the whole analyzed altitude interval they observed upward and downward fluxes from possible MW and NOGW, with some departures from linear polarization and presence of both types of waves. So they concluded that in the studied region there generally was a complex ensemble of types of waves and the scenarios could change according to the atmospheric layer and the background atmospheric situation. We found with WRF linearly polarized GW mainly over Andes and toward Southeast. NOGW were essentially detected by us over oceans and propagating upwards above the lower stratosphere, whereas a possible coexistence of both types of waves was noticed around the Drake Passage.

To further interpret the GW structures simulated by WRF, we use the small-volume few-wave decomposition technique S3D (Lehmann et al., 2012) that has already been widely and successfully used (e.g., Ern et al., 2017; Krasauskas et al., 2022; Preusse et al., 2014; Strube et al., 2021). This algorithm performs three-dimensional sinusoidal fits in small data cubes and contrary to the Fourier method it is not limited to a discrete frequency series. The algorithm identifies the oscillation that explains the most variance in the local three-dimensional temperature perturbation field. The outcome may include GW with wavelengths larger than the cube size. The output variables are functions of physical space that provide gridded information of the waves that are present.

In Figure 19, we show the results at 03 UTC on September 12 as a representation of the conditions around half of the flight time. Three

different altitudes have been used which roughly correspond to the tropopause, middle stratosphere, and lower mesosphere: 10, 30, and 55 km. Perturbation temperature amplitudes are shown separated for vertical wavelengths shorter and larger than 5 km (presumably NOGW and MW, henceforth VS and VL) which are determined with two different cube sizes. For VS waves, we used boxes of $93 \times 93 \times 2.5$ km^3 (respectively two horizontal and one vertical dimension). The cube size used to fit VL waves was $93 \times 93 \times 10.5$ km^3, which then made S3D more sensitive to larger vertical wavelengths. Thresholds for amplitude detection of the method were respectively set for the increasing heights at 0.5, 2, and 3K. At 10 km altitude, only VL are seen with horizontal wavelength shorter than 200 km and vertical wavelength shorter than 8 km. The distribution in terms of ground-based horizontal phase speed in direction of the wave vector is also exhibited (it will be negative whenever intrinsic phase speed and ground-based wave propagation are opposite). As expected for MW, the ground-based horizontal phase speed of VL is nearly centered around 0 (with a bias toward negative values). We assessed the significance of the spread and departure from zero of the phase speeds for both populations at the three heights. For VL, the standard deviation | mean at 10, 30, and 55 km are respectively (in m/s) 3.3 | −1.3, 6.0 | −6.9 and 10.3 | −5.2. For VS at 30 and 55 km (no waves at 10 km), we obtain 6.6 | −11.4 and 11.5 | −12.1. VL and VS have clearly distinct characteristics. At 30 km altitude, we see separate VS and VL waves on the right panel of the figure, but on the left side it rather seems to be a continuum. On the other hand, at 55 km height, both populations are discernible on the two panels and at 10 km altitude only one of them may be observed. We should therefore warn here that vertical wavelengths may change with height. So, keeping the 5 km cutoff for all altitudes may be somehow arbitrary or it may at least obscure the separation of the two wave types on the left panels. The right sides of the figure keep the separation more clearly along the three heights shown. The VL waves at 30 km altitude include larger horizontal and vertical wavelengths compared to 10 km height and exhibit a similar behavior regarding the phase speed, whereas VS waves possess up to 200 km horizontal wavelengths and a clear negative phase speed, indicating that they are not stationary MW. These negative values may be typical for a spontaneous imbalance source. The GW run intrinsically against the wind, but the ground-based phase propagates with the wind. A roughly similar scenario is observed at 55 km height but with the VL waves including even larger horizontal and vertical wavelengths. The latter fact is roughly in agreement with a general increase in the background horizontal winds from the lower layers up to about 40–45 km height according to WRF simulations (not shown for brevity) in the studied area and time. In general, temperature amplitudes of VL are seen to increase with altitude, whereas VS rather show maxima at 30 km. This reinforces the argument that they both represent different waves populations. Moreover, VS waves are here not detected in the lower atmosphere as it happened in Section 5.1 with the search of NOGW through GW polarization relations on WRF data. However, we should note that VS horizontal wavelengths are limited up to 200 km, but this aspect could be due to a possible S3D bias mentioned below regarding the finding of both types of waves.

Caution is needed in the interpretation of these results. The setup of S3D used here usually underestimates amplitudes. In addition, the method fits in every cube only the most significant wave. This may lead to a bias if one tries to quantify the types of GW that are present. As MW may have larger amplitudes than NOGW (compare, e.g., the corresponding PSD of horizontal velocity perturbation components in Figure 18 or temperature amplitude at 55 km height in Figure 19) they may be over-represented in the present analysis. We may assert that both types of GW exist in the studied region. Also, the sensitivity for wave detection changes with altitude and may be strongly dependent on the amplitude threshold that has been chosen at every level (note, e.g., that the number of markers against level in Figure 19 does not remain constant). We can therefore hardly ensure that we are following the same waves at increasing heights. However, possible stratospheric sources may lead to an increase of detected GW with height. In addition, Movie S1 showed that MW activity was lowering over time and this could also explain stronger waves higher up.

WRF configuration and studied phenomena in the present work are very similar to a recent study. However, time periods and observational platforms are different. We now briefly discuss how results from both works relate to each other. Kruse et al. (2022) used four atmospheric numerical models including WRF with tops near 80 km to analyze various MW cases over the Drake Passage, the Southern Andes, the Antarctic

Peninsula, and some remote islands in the Atlantic Ocean during 10 days of October 2010. Significant GW events were observed. The authors recalled that the importance of the momentum deposited by MW breaking with respect to the zonally averaged budget usually maximizes in the upper stratosphere and lower mesosphere according to standard drag parameterizations. The sponge layers near the tops of the four models significantly reduced wave amplitudes in the upper stratosphere and mesosphere. The conclusions of this work stated that the four models undervalued observed MW amplitudes and that even at 3 km horizontal resolution the small scales were not well resolved. They also found that MW with meridional propagation components may significantly enhance zonal drag over the Drake Passage. Quantitative validations of the models were performed against satellite observations in the stratosphere. In agreement with our results, that work finds that the zonal drag in the studied region may sometimes exceed -50 m s^{-1} d^{-1}, typically in some height ranges above 40 km. Their results also show that the meridional component is usually smaller than the zonal one. In addition, some vertical profiles show that local drag maxima may stay around the middle stratosphere and especially close to the stratopause. That work also sees in some cases a possible sign inversion height interval of the meridional drag around 40 and 60 km altitude. However, they do not find as our work a sign change of the zonal component in an interval around 40 km. We should consider that in both studies that have been here compared the space and time averaging procedures and the analyzed year and month are different. Kruse et al. (2022) include the meridional divergence of meridional flux of zonal momentum in evaluating the MW effect on large-scale zonal flow, which according to their results may have a significant effect at and below the polar jet maximum.

The performance of WRF with GW above very complex terrain has been here tested against onboard-based observations up to the mesosphere. *T*, *u*, and *v* behaviors are roughly reproduced. Variability over large spatial scales (but still pertaining to the GW regime) is better reconstructed by the model than over small distances. There is no good agreement in *w* between WRF and BAHAMAS but in a few notable cases. This is no surprise in relation to previous works. WRF and ALIMA show corresponding general features in *T* between 20 and 60 km, whereas *dT* patterns are similar but sometimes differ in amplitudes. The WRF and ALIMA outcomes show signatures of GW breaking and dissipation or secondary wave excitation at some nearly coincident stratospheric or mesospheric levels close to mountains and deep propagation in other parts. The drag produced above the whole studied area during the flight by WRF had comparable zonal and meridional negative components. The WRF drag general outlook (order of magnitude, sign, increasing and decreasing vertical intervals) resembles the seasonal profile obtained by a fixed lidar in this geographical region (Kaifler et al., 2020). There is a significant GW drag rise from WRF about 25 km height with a maximum around 50 km height, mainly at the beginning of the flight. Thereafter the values became less intense. About half of the drag may be attributed to the horizontal wavelengths shorter than 100 km (more likely MW than NOGW) according to WRF. However, the numerical model only partly resolves the spectrum of waves and it may have more difficulties in reproducing the smallest scales, so that fraction is likely an underestimate.

Appendix A: Some WRF Vertical Velocity Skill Tests

In the aim of testing whether a higher horizontal resolution of WRF leads to a closer agreement between observed and modeled vertical velocity we show results within domain d03 for one segment of leg 1 and another one from leg 2 which are mainly around Andes (Figure A1). The model was forced with NCEP/GDAS data. No approach between both data sources may be noticed in these additional results (compared with Figures 4 and 5). The PDF shape for WRF and BAHAMAS data is quite similar but it is necessary to keep in mind that for both the number of bins is the same but not the range of values, so the normalization process is different.
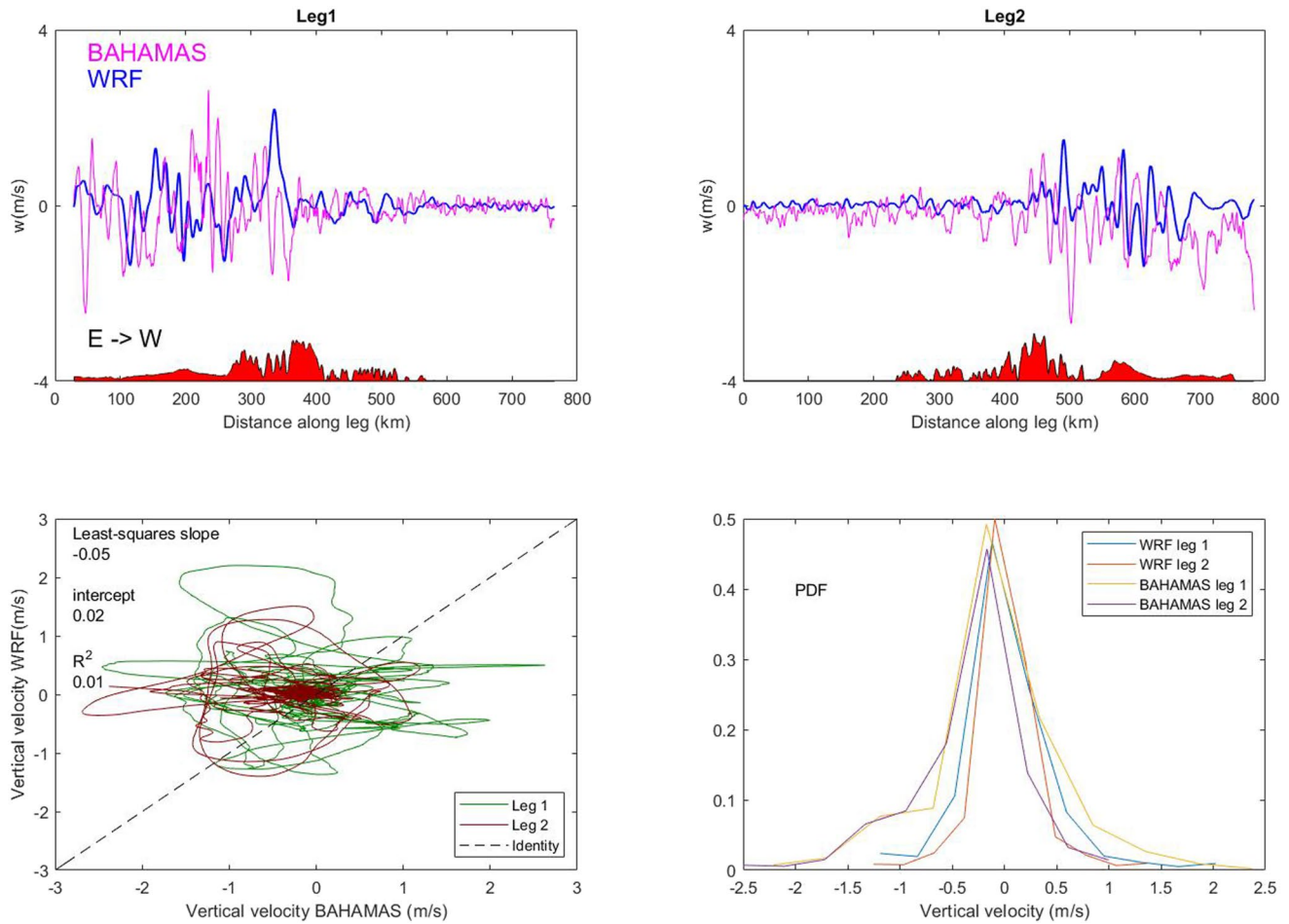
Figure A1. The two top panels show very high horizontal resolution (1 km) *w* WRF simulations in sectors of legs 1 and 2 around Andes. Topography is represented in red with an arbitrary scale. In the lower left panel, we compare the 1 km horizontal resolution data from WRF and BAHAMAS for both legs at the same time and position. Regression results and the identity line are included. On the lower right panel, we exhibit the probability density function of WRF and BAHAMAS data in both legs. Calculations for BAHAMAS and WRF have the same number of bins but different ranges in obtaining PDF (the former *w* extends over a larger interval).

From Figure 5, we may also conclude on *w* that in the analyzed scenario WRF seems to display essentially the effects of flow perturbations due to topography. Away from orography, the discrepancies are quite clear across a broad range of scales, but mainly among the smallest ones. These facts become clear when plotting PSD_w for WRF and BAHAMAS after dividing leg 6 into 2 halves, the first one above and close to topography and the second one over the ocean (Figure A2). Notice also that domain d02 model data are meaningless above wave number 0.17 1/km as the horizontal resolution is 3 km, whereas BAHAMAS results show no abrupt behavior change there.
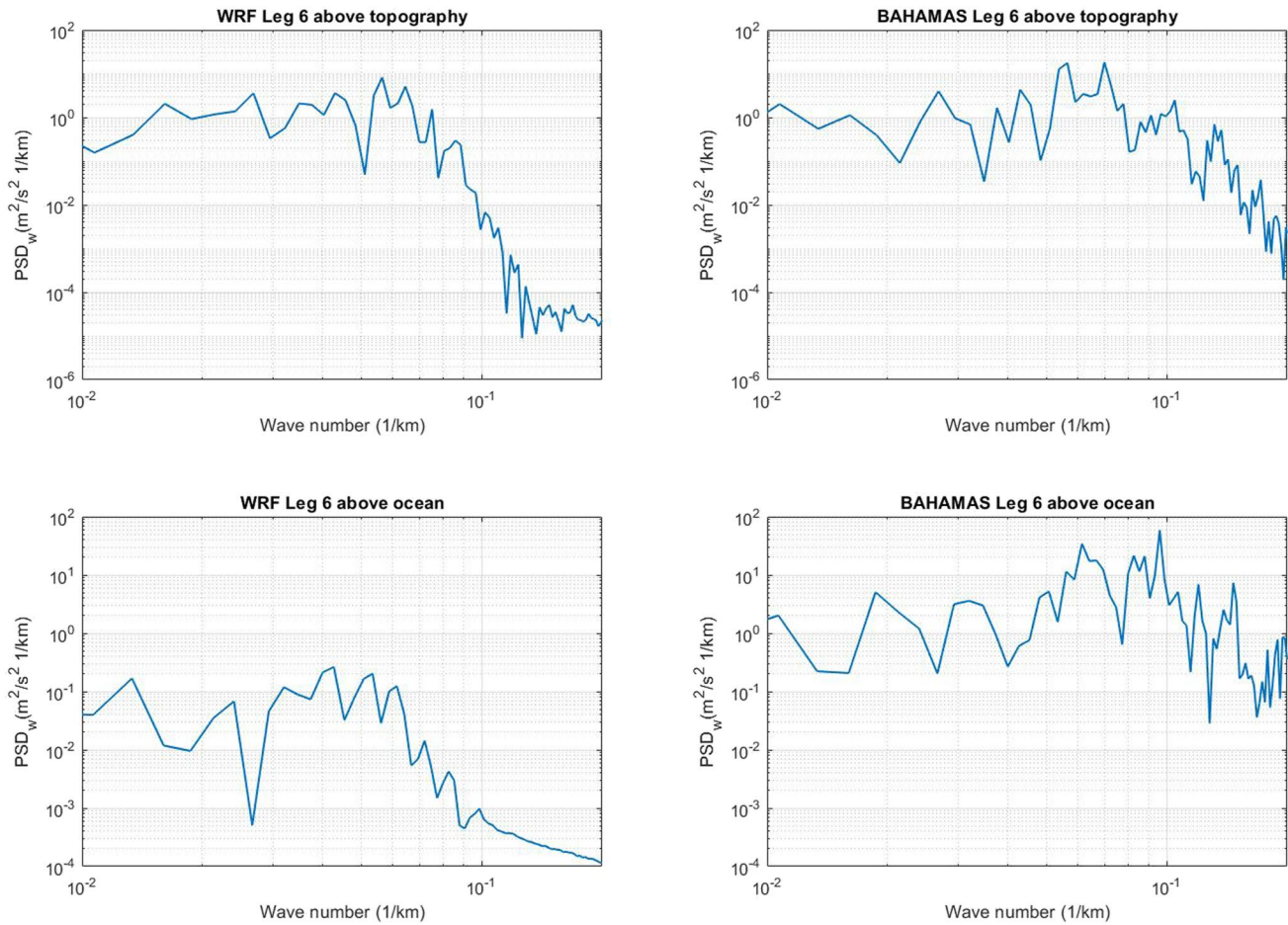
Figure A2. PSD_w for WRF and BAHAMAS data from leg 6 in a first segment above topography and surroundings and the remaining part over the ocean. Wave numbers are obtained from distances along the trajectory.

Data Availability Statement

ERA5 profiles were downloaded from https://cds.climate.copernicus.eu, whereas NCEP/GDAS data were obtained from https://rda.ucar.edu. BAHAMAS and ALIMA (2022) soundings for flight ST08 are available from https://doi.org/10.5281/zenodo.7246210. WRF (2022) simulations may be obtained from https://doi.org/10.5281/zenodo.6678395 (the three velocity components) and https://doi.org/10.5281/zenodo.6701414 (pressure and temperature).

References

Alexander, P., & de la Torre, A. (2010). A method to infer the three cartesian wavelengths of a mountain wave from three soundings. *Journal of Applied Meteorology and Climatology*, *49*, 2069–2074. https://doi.org/10.1175/2010JAMC2348.1

Alexander, P., de la Torre, A., & Llamedo, P. (2008). The interpretation of gravity waves signatures extracted from GPS radio occultations. *Journal of Geophysical Research*, *113*, D16117. https://doi.org/10.1029/2007JD009390

Alexander, P., Luna, D., Llamedo, P., & de la Torre, A. (2010). A gravity waves study close to the Andes mountains in Patagonia and Antarctica with GPS radio occultation observations. *Annales Geophysicae*, *28*, 587–595. https://doi.org/10.5194/angeo-28-587-2010

BAHAMAS and ALIMA. (2022). BAHAMAS and ALIMA. [Dataset]. https://doi.org/10.5281/zenodo.7246210

Becker, E., & Vadas, S. L. (2018). Secondary gravity waves in the winter mesosphere: Results from a high-resolution, gravity-wave resolving global circulation model. *Journal of Geophysical Research: Atmospheres*, *123*, 2605–2627. https://doi.org/10.1002/2017JD027460

Becker, E., Vadas, S. L., Bossert, K., Harvey, L., Zülicke, C., & Hoffmann, L. (2022). A high-resolution whole-atmosphere model with resolved gravity waves and specified large-scale dynamics in the troposphere and stratosphere. *Journal of Geophysical Research: Atmospheres*, *127*, e2021JD035018. https://doi.org/10.1029/2021JD035018

de la Torre, A., & Alexander, P. (1995). The interpretation of wavelengths and periods as measured from atmospheric balloons. *Journal of Applied Meteorology*, *3*, 2747–2754. https://doi.org/10.1175/1520-0450(1995)034<2747:TIOWAP>2.0.CO;2

de la Torre, A., Alexander, P., Hierro, R., Llamedo, P., Rolla, A., Schmidt, T., & Wickert, J. (2012). Large-amplitude gravity waves above the southern Andes, the Drake Passage, and the Antarctic Peninsula. *Journal of Geophysical Research*, *117*, D02106. https://doi.org/10.1029/2011JD016377

de la Torre, A., Alexander, P., Llamedo, P., Menéndez, C., Schmidt, T., & Wickert, J. (2006). Gravity waves above the Andes detected from GPS radio occultation temperature profiles: Jet mechanism? *Geophysical Research Letters*, *33*, L24810. https://doi.org/10.1029/2006GL027343

de la Torre, A., Alexander, P., Schmidt, T., Llamedo, P., & Hierro, R. (2018). On the distortions in calculated GW parameters during slanted atmospheric soundings. *Atmospheric Measurement Techniques*, *11*, 1363–1375. https://doi.org/10.5194/amt-11-1363-2018

de la Torre, A., Alexander, P., Macros, T., Hierro, R., Llamdo, P., Hormeachea, J. L., et al. (2023). A spectral rotary analysis of gravity waves: An application during one of the SOUTHTRAC flights. *Journal of Geophysical Research: Atmospheres*, *128*, e2022JD037139. https://doi.org/10.1029/2022JD037139

Dörnbrack, A., Bechtold, P., & Schumann, U. (2022). High-resolution aircraft observations of turbulence and waves in the free atmosphere and comparison with global model predictions. *Journal of Geophysical Research*, *127*, e2022JD036654. https://doi.org/10.1029/2022JD036654

Dörnbrack, A., Birner, T., Fix, A., Flentje, H., Meister, A., Schmid, H., et al. (2002). Evidence for inertia gravity waves forming polar stratospheric clouds over Scandinavia. *Journal of Geophysical Research*, *107*, 8287. https://doi.org/10.1029/2001JD000452

Dörnbrack, A., Kaifler, B., Kaifler, N., Rapp, M., Wildmann, N., Garhammer, M., et al. (2020). Unusual appearance of mother-of-pearl clouds above El Calafate, Argentina (50°21S, 72°16W). *Weather*, *75*, 378–388. https://doi.org/10.1002/wea.3863

Eckermann, S. D., Doyle, J. D., Reinecke, P. A., Reynolds, C. A., Smith, R. B., Fritts, D. C., & Dörnbrack, A. (2019). Stratospheric gravity wave products from satellite infrared nadir radiances in the planning, execution, and validation of aircraft measurements during DEEPWAVE. *Journal of Applied Meteorology and Climatology*, *58*, 2049–2075. https://doi.org/10.1175/JAMC-D-19-0015.1

Ehard, B., Kaifler, B., Kaifler, N., & Rapp, M. (2015). Evaluation of methods for gravity wave extraction from middle-atmospheric lidar temperature measurements. *Atmospheric Measurement Techniques*, *8*, 4645–4655. https://doi.org/10.5194/amt-8-4645-2015

Eliassen, A., & Palm, E. (1960). On the transfer of energy in stationary mountain waves. *Geofysiske Publikasjoner*, *22*, 1–23.

Ern, M., Hoffmann, L., & Preusse, P. (2017). Directional gravity wave momentum fluxes in the stratosphere derived from high-resolution AIRS temperature data. *Geophysical Research Letters*, *44*, 475–485. https://doi.org/10.1002/2016GL072007

Ern, M., Preusse, P., Alexander, M. J., & Warner, C. D. (2004). Absolute values of gravity wave momentum flux derived from satellite data. *Journal of Geophysical Research*, *109*, D20103. https://doi.org/10.1029/2004JD004752

Ern, M., Trinh, Q. T., Preusse, P., Gille, J. C., Mlynczak, M. G., Russell, J. M., III, & Riese, M. (2018). GRACILE: A comprehensive climatology of atmospheric gravity wave parameters based on satellite limb soundings. *Earth System Science Data*, *10*, 857–892. https://doi.org/10.5194/essd-10-857-2018

Fritts, D. C., & Alexander, J. (2003). Gravity wave dynamics and effects in the middle atmosphere. *Reviews of Geophysics*, *41*, 1003. https://doi.org/10.1029/2001RG000106

Fritts, D. C., Smith, R. B., Taylor, M. J., Doyle, J. D., Eckermann, S. D., Dörnbrack, A., et al. (2016). The Deep Propagating Gravity Wave Experiment (DEEPWAVE): An airborne and ground-based exploration of gravity wave propagation and effects from their sources throughout the lower and middle atmosphere. *Bulletin of the American Meteorological Society*, *97*, 425–453. https://doi.org/10.1175/BAMS-D-14-00269.1

Garcia, R. R., Smith, A. K., Kinnison, D. E., de la Cámara, A., & Murphy, D. J. (2017). Modification of the gravity wave parameterization in the whole atmosphere community climate model: Motivation and results. *Journal of the Atmospheric Sciences*, *74*, 275–291. https://doi.org/10.1175/JAS-D-16-0104.1

Geldenhuys, M., Kaifler, B., Preusse, P., Ungermann, J., Alexander, P., Krasaukas, L., et al. (2023). Observations of gravity wave refraction and its causes and consequences. *Journal of Geophysical Research: Atmospheres*, *128*, e2022JD036830. https://doi.org/10.1029/2022JD036830

Geldenhuys, M., Preusse, P., Krisch, I., Zülicke, C., Ungermann, J., Ern, M., et al. (2021). Orographically induced spontaneous imbalance within the jet causing a large-scale gravity wave event. *Atmospheric Chemistry and Physics*, *21*, 10393–10412. https://doi.org/10.5194/acp-21-10393-2021

Giez, A., Mallaun, C., Nenakhov, V., & Zöger, M. (2021). Calibration of a nose boom mounted airflow sensor on an atmospheric research aircraft by inflight maneuvers, DLR-FB-2021-17. Retrieved from https://elib.dlr.de/145969

Giez, A., Mallaun, C., Zöger, M., Dörnbrack, A., & Schumann, U. (2017). Static pressure from aircraft trailing-cone measurements and numerical weather prediction analysis. *Journal of Aircraft*, *54*, 1728–1737. https://doi.org/10.2514/1.C034084

Gill, A. E. (1982). *Atmosphere and ocean dynamics*. Academic Press.

Grinsted, A., Moore, J. C., & Jevrejeva, S. (2004). Application of the cross wavelet transform and wavelet coherence to geophysical time series. *Nonlinear Processes in Geophysics*, *11*, 561–566. https://doi.org/10.5194/npg-11-561-2004

Hendricks, E. A., Doyle, J. D., Eckermann, S. D., Jiang, Q., & Reinecke, P. A. (2014). What is the source of the stratospheric gravity wave belt in austral winter? *Journal of the Atmospheric Sciences*, *71*, 1583–1592. https://doi.org/10.1175/JAS-D-13-0332.1

Hertzog, A., Boccara, G., Vincent, R. A., Vial, F., & Cocquerez, P. (2008). Estimation of gravity wave momentum flux and phase speeds from quasi-Lagrangian stratospheric balloon flights. Part II: Results from the Vorcore campaign in Antarctica. *Journal of the Atmospheric Sciences*, *65*, 3056–3070. https://doi.org/10.1175/2008JAS2710.1

Hindley, N. P., Wright, C. J., Smith, N. D., & Mitchell, N. J. (2015). The southern stratospheric gravity wave hotspot: Individual waves and their momentum fluxes measured by COSMIC GPS-RO. *Atmospheric Chemistry and Physics*, *15*, 7797–7818. https://doi.org/10.5194/acp-15-7797-2015

Hines, C. O., & Reddy, C. A. (1967). On the propagation of atmospheric gravity waves through regions of wind shear. *Journal of Geophysical Research*, *72*, 1015–1034. https://doi.org/10.1029/JZ072i003p01015

Hoffmann, L., Grimsdell, A. W., & Alexander, M. J. (2016). Stratospheric gravity waves at Southern Hemisphere orographic hotspots: 2003–2014 AIRS/Aqua observations. *Atmospheric Chemistry and Physics*, *16*, 9381–9397. https://doi.org/10.5194/acp-16-9381-2016

Hoffmann, L., Xue, X., & Alexander, M. J. (2013). A global view of stratospheric gravity wave hotspots located with atmospheric infrared sounder observations. *Journal of Geophysical Research: Atmospheres*, *118*, 416–434. https://doi.org/10.1029/2012JD018658

John, S. R., & Kumar, K. K. (2013). A discussion on the methods of extracting gravity wave perturbations from space-based measurements. *Geophysical Research Letters*, *40*, 2406–2410. https://doi.org/10.1002/grl.50451

Kaifler, B., Büdenbender, C., Mahnke, P., Damm, M., Sauder, D., Kaifler, N., & Rapp, M. (2017). Demonstration of an iron fluorescence lidar operating at 372 nm wavelength using a newly-developed Nd:YAG laser. *Optics Letters*, *42*, 2858–2861. https://doi.org/10.1364/OL.42.002858

Kaifler, B., & Kaifler, N. (2021). A Compact Rayleigh Autonomous Lidar (CORAL) for the middle atmosphere. *Atmospheric Measurement Techniques*, *14*, 1715–1732. https://doi.org/10.5194/amt-14-1715-2021

Kaifler, N., Kaifler, B., Dörnbrack, A., Rapp, M., Hormaechea, J. L., & de la Torre, A. (2020). Lidar observations of large-amplitude mountain waves in the stratosphere above Tierra del Fuego, Argentina. *Scientific Reports*, *10*, 14529. https://doi.org/10.1038/s41598-020-71443-7

Kogure, M., Yue, J., Nakamura, T., Hoffmann, L., Vadas, S. L., Tomikawa, Y., et al. (2020). First direct observational evidence for secondary gravity waves generated by mountain waves over the Andes. *Geophysical Research Letters*, *47*, e2020GL088845. https://doi.org/10.1029/2020GL088845

Krasauskas, L., Kaifler, B., Rhode, S., Ungermann, J., Woiwode, W., & Preusse, P. (2022). Oblique propagation of mountain waves to the upwind side of the Andes observed by GLORIA and ALIMA during the SouthTRAC campaign. https://doi.org/10.1002/essoar.10512325.1

Kruse, C. G., Alexander, M. J., Hoffmann, L., van Niekerk, A., Polichtchouk, I., Bacmeister, J. T., et al. (2022). Observed and modeled mountain waves from the surface to the mesosphere near the Drake Passage. *Journal of the Atmospheric Sciences*, *79*, 909–932. https://doi.org/10.1175/JAS-D-21-0252.1

Kruse, C. G., & Smith, R. B. (2015). Gravity wave diagnostics and characteristics in mesoscale fields. *Journal of the Atmospheric Sciences*, *72*, 4372–4392. https://doi.org/10.1175/JAS-D-15-0079.1

Kruse, C. G., Smith, R. B., & Eckermann, S. D. (2016). The midlatitude lower-stratospheric mountain wave "valve layer". *Journal of the Atmospheric Sciences*, *73*, 5081–5100. https://doi.org/10.1175/JAS-D-16-0173.1

Lehmann, C. I., Kim, Y.-H., Preusse, P., Chun, H.-Y., Ern, M., & Kim, S.-Y. (2012). Consistency between Fourier transform and small-volume few-wave decomposition for spectral and spatial variability of gravity waves above a typhoon. *Atmospheric Measurement Techniques*, *5*, 1637–1651. https://doi.org/10.5194/amt-5-1637-2012

Lindzen, R. S. (1973). Wave-mean flow interactions in the upper atmosphere. *Boundary-Layer Meteorology*, 4, 327–343. https://doi.org/10.1007/BF02265242

Llamedo, P., Salvador, J., de la Torre, A., Quiroga, J., Alexander, P., Hierro, R., et al. (2019). 11 years of Rayleigh lidar observations of gravity wave activity above the southern tip of South America. *Journal of Geophysical Research: Atmospheres*, *124*, 451–467. https://doi.org/10.1029/2018JD028673

Lu, X., Chu, X., Li, H., Chen, C., Smith, J. A., & Vadas, S. L. (2017). Statistical characterization of high-to-medium frequency mesoscale gravity waves by lidar-measured vertical winds and temperatures in the MLT. *Journal of Atmospheric and Solar-Terrestrial Physics*, *162*, 3–15. https://doi.org/10.1016/j.jastp.2016.10.009

McLandress, C., Shepherd, T. G., Polavarapu, S., & Beagley, S. R. (2012). Is missing orographic gravity wave drag near 60°S the cause of the stratospheric zonal wind biases in chemistry–climate models? *Journal of the Atmospheric Sciences*, *69*, 802–818. https://doi.org/10.1175/JAS-D-11-0159.1

Nappo, C. J. (2012). *An introduction to atmospheric gravity waves* (2nd ed.). Academic Press.

Nash, E. R., Newman, P. A., Rosenfield, J. E., & Schoeberl, M. R. (1996). An objective determination of the polar vortex using Ertel's potential vorticity. *Journal of Geophysical Research*, *101*, 9471–9478. https://doi.org/10.1029/96JD00066

Plougonven, R., Hertzog, A., & Alexander, M. J. (2015). Case studies of nonorographic gravity waves over the southern ocean emphasize the role of moisture. *Journal of Geophysical Research: Atmospheres*, *120*, 1278–1299. https://doi.org/10.1002/2014JD022332

Plougonven, R., Hertzog, A., & Guez, L. (2013). Gravity waves over Antarctica and the Southern Ocean: Consistent momentum fluxes in mesoscale simulations and stratospheric balloon observations. *Quarterly Journal of the Royal Meteorological Society*, *139*, 101–118. https://doi.org/10.1002/qj.1965

Plougonven, R., Hertzog, A., & Teitelbaum, H. (2008). Observations and simulations of a large-amplitude mountain wave breaking over the Antarctic Peninsula. *Journal of Geophysical Research*, *113*, D16113. https://doi.org/10.1029/2007JD009739

Plougonven, R., Teitelbaum, H., & Zeitlin, V. (2003). Inertia-gravity wave generation by the tropospheric midlatitude jet as given by the Fronts and Atlantic Storm-Track Experiment radio soundings. *Journal of Geophysical Research*, *108*, 4686. https://doi.org/10.1029/2003JD003535

Plougonven, R., & Zhang, F. (2014). Internal gravity waves from atmospheric jets and fronts. *Reviews of Geophysics*, *52*, 33–76. https://doi.org/10.1002/2012RG000419

Preusse, P., Ern, M., Bechtold, P., Eckermann, S. D., Kalisch, S., Trinh, Q. T., & Riese, M. (2014). Characteristics of gravity waves resolved by ECMWF. *Atmospheric Chemistry and Physics*, *14*, 10483–10508. https://doi.org/10.5194/acp-14-10483-2014

Preusse, P., Schroeder, S., Hoffmann, L., Ern, M., Friedl-Vallon, F., Ungermann, J., et al. (2009). New perspectives on gravity wave remote sensing by spaceborne infrared limb imaging. *Atmospheric Measurement Techniques*, *2*, 299–311. https://doi.org/10.5194/amt-2-299-2009

Queney, P. (1948). The problem of air flow over mountains: A summary of theoretical studies. *Bulletin of the American Meteorological Society*, *29*, 16–26. https://doi.org/10.1175/1520-0477-29.1.16

Rapp, M., Kaifler, B., Dörnbrack, A., Gisinger, S., Mixa, T., Reichert, R., et al. (2021). SOUTHTRAC-GW: An airborne field campaign to explore gravity wave dynamics at the world's strongest hotspot. *Bulletin of the American Meteorological Society*, *102*, E871–E893. https://doi.org/10.1175/BAMS-D-20-0034.1

Reichert, R., Kaifler, B., Kaifler, N., Dörnbrack, A., Rapp, M., & Hormaechea, J. L. (2021). High-cadence lidar observations of middle atmospheric temperature and gravity waves at the Southern Andes hot spot. *Journal of Geophysical Research*, *126*, e2021JD034683. https://doi.org/10.1029/2021JD034683

Sato, K., Tateno, S., Watanabe, S., & Kawatani, Y. (2012). Gravity wave characteristics in the Southern Hemisphere revealed by a high-resolution middle-atmosphere general circulation model. *Journal of the Atmospheric Sciences*, *69*, 1378–1396. https://doi.org/10.1175/JAS-D-11-0101.1

Satomura, T., & Sato, K. (1999). Secondary generation of gravity waves associated with the breaking of mountain waves. *Journal of the Atmospheric Sciences*, *56*, 3847–3858. https://doi.org/10.1175/1520-0469(1999)056<3847:SGOGWA>2.0.CO;2

Schoeberl, M. R., & Newman, P. A. (2015). Encyclopedia of atmospheric sciences. In G. R. North, J. Pyle, & F. Zhang (Eds.), *Chapter middle atmosphere: Polar vortex* (2nd ed., Vol. 4, pp. 12–17). Academic Press. https://doi.org/10.1016/B978-0-12-382225-3.00228-0

Scorer, R. S. (1949). Theory of waves in the lee of mountains. *Quarterly Journal of the Royal Meteorological Society*, *75*, 41–56. https://doi.org/10.1002/qj.49707532308

Skamarock, W., & Klemp, J. B. (2008). A time-split nonhydrostatic atmospheric model for weather research and forecasting applications. *Journal of Computational Physics*, *227*, 3465–3485. https://doi.org/10.1016/j.jcp.2007.01.037

Smith, R. B., Nugent, A. D., Kruse, C. G., Fritts, D. C., Doyle, J. D., Eckermann, S. D., et al. (2016). Stratospheric gravity wave fluxes and scales during DEEPWAVE. *Journal of the Atmospheric Sciences*, *73*(7), 2851–2869. https://doi.org/10.1175/JAS-D-15-0324.1

Smith, R. B., Woods, B. K., Jensen, J., Cooper, W. A., Doyle, J. D., Jiang, Q., & Grubišić, V. (2008). Mountain waves entering the stratosphere. *Journal of the Atmospheric Sciences*, *65*, 2543–2562. https://doi.org/10.1175/2007JAS2598.1

Strube, C., Preusse, P., Ern, M., & Riese, M. (2021). Propagation paths and source distributions of resolved gravity waves in ECMWF-IFS analysis fields around the southern polar night jet. *Atmospheric Chemistry and Physics*, *21*, 18641–18668. https://doi.org/10.5194/acp-21-18641-2021

Torrence, C., & Compo, G. P. (1998). A practical guide to wavelet analysis. *Bulletin of the American Meteorological Society*, *79*, 61–78. https://doi.org/10.1175/1520-0477(1998)079<0061:APGTWA>2.0.CO;2

Uccellini, L. W., & Koch, S. E. (1987). The synoptic settings and possible energy sources for mesoscale wave disturbances. *Monthly Weather Review*, *115*, 721–729. https://doi.org/10.1175/1520-0493(1987)115<0721:TSSAPE>2.0.CO;2

Vadas, S. L. (2013). Compressible f-plane solutions to body forces, heatings, and coolings, and application to the primary and secondary gravity waves generated by a deep convective plume. *Journal of Geophysical Research: Space Physics*, *118*, 2377–2397. https://doi.org/10.1002/jgra.50163

Vadas, S. L., & Becker, E. (2018). Numerical modeling of the excitation, propagation, and dissipation of primary and secondary gravity waves during wintertime at McMurdo Station in the Antarctic. *Journal of Geophysical Research: Atmospheres*, *123*, 9326–9369. https://doi.org/10.1029/2017JD027974

Vadas, S. L., & Becker, E. (2019). Numerical modeling of the generation of tertiary gravity waves in the mesosphere and thermosphere during strong mountain wave events over the Southern Andes. *Journal of Geophysical Research: Space Physics*, *124*, 7687–7718. https://doi.org/10.1029/2019JA026694

Vadas, S. L., & Nicolls, M. J. (2012). The phases and amplitudes of gravity waves propagating and dissipating in the thermosphere: Theory. *Journal of Geophysical Research*, *117*, A05322. https://doi.org/10.1029/2011JA017426

Vadas, S. L., Zhao, J., Chu, X., & Becker, E. (2018). The excitation of secondary gravity waves from local body forces: Theory and observation. *Journal of Geophysical Research: Atmospheres*, *123*, 9296–9325. https://doi.org/10.1029/2017JD027970

Wagner, J., Dörnbrack, A., Rapp, M., Gisinger, S., Ehard, B., Bramberger, M., et al. (2017). Observed versus simulated mountain waves over Scandinavia – Improvement of vertical winds, energy and momentum fluxes by enhanced model resolution? *Atmospheric Chemistry and Physics*, *17*, 4031–4052. https://doi.org/10.5194/acp-17-4031-2017

Wildmann, N., Eckert, R., Dörnbrack, A., Gisinger, S., van Niekerk, A., Ohlmann, K., & Rapp, M. (2021). In situ measurements of wind and turbulence by a motor glider in the Andes. *Journal of Atmospheric and Oceanic Technology*, 38921–38935. https://doi.org/10.1175/JTECH-D-20-0137.1

WRF. (2022). WRF. [Dataset]. https://doi.org/10.5281/zenodo.6678395

Wright, C., Hindley, N., Moss, A., & Mitchell, N. (2016). Multi-instrument gravity-wave measurements over Tierra del Fuego and the Drake Passage—Part 1: Potential energies and vertical wavelengths from AIRS, COSMIC,HIRDLS, MLS-Aura, SAAMER, SABER and radiosondes. *Atmospheric Measurement Techniques*, *9*, 877–908. https://doi.org/10.5194/amt-9-877-2016

Zhao, J., Chu, X., Chen, C., Lu, X., Fong, W., Yu, Z., et al. (2017). Lidar observations of stratospheric gravity waves from 2011 to 2015 at McMurdo (77.84oS, 166.69oE), Antarctica: 1. Vertical wavelengths, periods, and frequency and vertical wavenumber spectra. *Journal of Geophysical Research: Atmospheres*, *122*, 5041–5062. https://doi.org/10.1002/2016JD026368